Atmos. Meas. Tech. Discuss., 7, 8881–8926, 2014
www.atmos-meas-tech-discuss.net/7/8881/2014/
doi:10.5194/amtd-7-8881-2014

Atmospheric Measurement Techniques Discussions

Profiling of fine- and coarse-mode particles with LIRIC (LIdar/Radiometer Inversion Code)

M. R. Perrone[1], P. Burlizzi[1], F. De Tomasi[1], and A. Chaikovsky[2]

[1]Matematical and Physical Department, Universita' del Salento, 73100 Lecce, Italy
[2]Institute of Physics, National Academy of Science, Minsk, Belarus

Received: 30 June 2014 – Accepted: 1 August 2014 – Published: 27 August 2014

Correspondence to: M. R. Perrone (perrone@le.infn.it)

Published by Copernicus Publications on behalf of the European Geosciences Union.

Abstract

The paper investigates numerical procedures that allow determining the dependence on altitude of aerosol properties from multi wavelength elastic lidar signals. In particular, the potential of the LIdar/Radiometer Inversion Code (LIRIC) to retrieve the vertical profiles of fine and coarse-mode particles by combining 3-wavelength lidar measurements and collocated AERONET (AErosol RObotic NETwork) sun/sky photometer measurements is investigated. The used lidar signals are at 355, 532 and 1064 nm. Aerosol extinction coefficient (α_L), lidar ratio (LR_L), and Ångstrom exponent ($Å_L$) profiles from LIRIC are compared with the corresponding profiles (α, LR, and Å) retrieved from a Constrained Iterative Inversion (CII) procedure to investigate the LIRIC retrieval ability. Then, an aerosol classification framework which relies on the use of a graphical framework and on the combined analysis of the Ångstrom exponent (at the 355 and 1064 nm wavelength pair, Å(355, 1064)) and its spectral curvature ($\Delta Å$ = Å(355, 532)–Å(532, 1064)) is used to investigate the ability of LIRIC to retrieve vertical profiles of fine and coarse-mode particles. The Å-$\Delta Å$ aerosol classification framework allows estimating the dependence on altitude of the aerosol fine modal radius and of the fine mode contribution to the whole aerosol optical thickness, as discussed in Perrone et al. (2014). The application of LIRIC to three different aerosol scenarios dealing with aerosol properties dependent on altitude has revealed that the differences between α_L and α vary with the altitude and on average increase with the decrease of the lidar signal wavelength. It has also been found that the differences between $Å_L$ and corresponding Å values vary with the altitude and the wavelength pair. The sensitivity of Ångstrom exponents to the aerosol size distribution which vary with the wavelength pair was responsible for these last results. The aerosol classification framework has revealed that the deviations between LIRIC and the corresponding CII-procedure retrieval products are due to the fact that LIRIC does not allow to the modal radius of fine mode particles to vary with the altitude. It is shown that this represents the main source of uncertainties in LIRIC results. The plot on the graphical framework of the Å-$\Delta Å$ data

AMTD
7, 8881–8926, 2014

points retrieved from the CII-procedure has indicated that the fine-mode-particle modal radius can vary with altitude when particles from different sources and/or from different advection routes contribute to the aerosol load. Analytical back trajectories combined with linear particle depolarization ratio profiles from lidar measurements at 355 nm and dust concentrations from the Barcelona Supercomputing Center-Dust REgional Atmospheric Model (BSC-DREAM) have been used to demonstrate the dependence on altitude of the aerosol properties.

1 Introduction

The impact of aerosol on climate is widely recognized and several efforts have been undertaken in the last years to characterize aerosol optical and microphysical properties and estimate aerosol direct and indirect radiative effects. Ground and satellite based remote sensing techniques have been developed to characterize aerosol properties from the ground up to the top of the atmosphere. Satellite-based observations provide global monitoring of the aerosol properties. On the contrary, ground-based observations are punctual but, they can allow a more detailed and accurate characterization of the aerosol optical and microphysical properties. Ground-based networks with similar remote-sensing devices and standardized data processing procedures have been developed to partially overcome the local nature of ground-based observations. The AErosol RObotic NETwork (AERONET, Holben et al., 1998) and the European Aerosol Research LIdar NETwork (EARLINET, Matthias et al., 2004) represent two typical examples. AERONET is a network of sun/sky photometers coordinated by NASA, operating on global scale. Column-integrated aerosol optical and microphysical properties are retrieved from AERONET sun/sky photometer observations (Dubovik and King, 2000; Dubovik et al., 2006, and references therein). EARLINET is the European aerosol lidar network, established in 2000, with the main goal of deriving long time series of the aerosol vertical distribution and providing a comprehensive, quantitative, and statistically significant data base for the aerosol distribution over Europe. Lidars

AMTD
7, 8881–8926, 2014

represent nowadays the best devices to retrieve aerosol vertical profiles. Aerosol effects on climate depend on the vertical distribution of the aerosol optical and microphysical properties (e.g. Perrone et al., 2012). As a consequence, several numerical approaches have been developed to invert aerosol extinction (α) and backscatter (β) coefficients retrieved from lidar measurements at multiple wavelengths to particle parameters (Veselovskii et al., 2010, 2012; Müller et al., 2013 and references therein): the higher the number of the input parameters the greater the number and the accuracy of the aerosol optical and microphysical properties that are derived. Multi-wavelength Raman lidars equipped with a depolarization (δ) channel are nowadays the most advanced lidar systems since they are generally equipped with ($3\beta + 2\alpha + 1\delta$) optical channels, as required in some advanced inversion procedures of lidar signals (e.g. Müller et al., 2013). However, most Raman lidars are designed for night time operation and they can only provide elastic lidar signals during daytime, as the lidar system used in this study (e.g. De Tomasi et al., 2006). In addition, it would be highly desirable to reduce the number of optical channels in some lidar experiments. Therefore, numerical procedures only based on elastic lidar signals have been developed to characterize the dependence on altitude of aerosol properties. Ansmann et al. (2012) have proposed the single-wavelength POLIPHON (POlarization LIdar PHOtometer Networking) technique for the retrieval of volume and mass concentration profiles for fine and coarse mode particles. This method is based on the measured height profile of the particle depolarization ratio to separate coarse dust from the residual aerosol particles (Wagner et al., 2013). A method which relies on the use of a graphical framework and on the combined analysis of the Angstrom exponent (at the 355 and 1064 nm wavelength pair, Å(355, 1064)) and its spectral curvature (ΔÅ = Å(355, 532)–Å(532, 1064)), calculated from the lidar extinction profiles at 355, 532, and 1064 nm, respectively, has recently been used by Perrone et al. (2014) to estimate the dependence on altitude of the aerosol fine mode radius (R_f) and of the fine mode contribution (η) to the aerosol optical thickness (AOT). This method is denoted as Å-ΔÅ graphical method. Chaikovsky et al. (2012) have developed a numerical tool (LIRIC, LIdar/Radiometer Inversion Code) to retrieve

AMTD
7, 8881–8926, 2014

vertically resolved aerosol microphysical properties by combining backscatter coefficient measurements at 3 wavelengths and sun/sky radiance measurements. This activity has been performed in the frame of the European Project Aerosol, Clouds, and Trace gases Research InfraStructure Network (ACTRIS, http://www.actris.net/) with the main aim of integrating sun/sky photometer and lidar measurements from AERONET and EARLINET, respectively. The GARRLiC (Generalized Aerosol Retrieval from Radiometer and Lidar Combined data) approach recently proposed by Lopatin et al. (2013) pursues even deeper synergy of lidar and radiometer data in the retrievals. Wagner et al. (2013) have recently evaluated the LIRIC performance to determine microphysical properties of volcanic and desert dust. To this end, LIRIC profiles of particle mass concentrations for the coarse-mode as well as for the non-spherical particle fraction have been compared with results for the non-spherical particle fraction from the POLIPHON method. The LIRIC spheroidal-particle model was considered as main source of uncertainties in the LIRIC results.

The main goal of this study is to contribute to the characterization and development of numerical procedures based on multi wavelength elastic lidar signals, to characterize the dependence on altitude of aerosol properties, since most of the multi wavelength lidar systems can only provide elastic lidar signals during the daytime operation. To this end, the potential of LIRIC to retrieve vertical profiles of fine- and coarse-mode particle volume concentrations by combining AERONET sun/sky photometer aerosol products and collocated in space and time 3-wavelength elastic lidar signals is investigated in this paper. More specifically, lidar measurements at 355, 532 and 1064 nm and sun/sky radiometer measurements performed at the Mathematics and Physics Department of Universita' del Salento, in south eastern Italy are used in this study. Aerosol from continental Europe, the Atlantic, northern Africa, and the Mediterranean Sea are often advected over south eastern Italy and as a consequence, mixed advection patterns leading to aerosol properties varying with altitude are dominant (e.g. Perrone et al., 2014). Three study cases representative of aerosol loads affected by different sources are analyzed to test the LIRIC retrieval ability. To this end, extinction,

AMTD
7, 8881–8926, 2014

lidar ratio, and Angstrom coefficient profiles from LIRIC are first compared with the corresponding profiles retrieved from a constrained iterative inversion procedure (Perrone et al., 2014). Then, the Å-ΔÅ graphical method (Perrone et al., 2014) is used to evaluate the potential of LIRIC to retrieve vertical profiles of fine- and coarse-mode particle volume concentrations and to understand the differences between LIRIC and the retrievals from the constrained iterative inversion (CII) procedure. Depolarization lidar measurements at 355 nm, analytical backtrajectories, and dust concentrations from the BSC-DREAM model (http://www.bsc.es/earth-sciences/mineral-dust-forecast-system/bsc-dream8b-forecast/north-africa-europe-and-middle-ea-0) are used to understand/support the change with altitude of the aerosol fine modal radius and of the fine mode fraction resulting from the Å-ΔÅ graphical method. A short overview of LIRIC, the 3 wavelength lidar system, the constrained iterative inversion procedure, and the Å-ΔÅ graphical method is given in Sect. 2. Results are presented and discussed in detail in Sect. 3. Summary and conclusion are given in Sect. 4.

2 Methods

2.1 The LIRIC tool

The basic structure of LIRIC is presented and discussed in Chaikovsky et al. (2012) and Wagner et al. (2013). A short overview of LIRIC features is reported in this section. AERONET inversion products and collocated background-corrected, elastically-backscattered, lidar signals $P(\lambda_i, z)$ at three different wavelengths λ_i and at the altitude z represent the input data set for LIRIC. More specifically, LIRIC has been designed for the analysis of the lidar signals at 355, 532, and 1064 nm in the simplified retrieval mode which allows retrieving two aerosol mode: fine and coarse. If polarization lidar measurements at 532 nm are also available LIRIC can operate in the polarimetric mode, which allows retrieving three aerosol modes: fine, coarse spherical and coarse spheroid. The LIRIC simplified retrieval mode is used in this study since polarization

AMTD
7, 8881–8926, 2014

lidar measurements at 532 nm are not available. The minimum measurement height z_o which depends on the lidar field of view and the lidar signal reference-height z_f must also be provided. Note that from the ground up to $z = z_o$, LIRIC assumes constant aerosol optical and microphysical properties and hence, height-independent particle backscatter and extinction coefficients. LIRIC searches for particle lidar profiles that best match the AERONET-derived column volume concentrations to retrieve the vertical profiles of fine $C_f(\lambda_i, z)$ and coarse $C_c(\lambda_i, z)$ particle volume concentrations and the height-independent volume-specific backscatter $b_m(\lambda_i)$ and extinction $a_m(\lambda_i)$ coefficients of the fine (m = f) and coarse (m = c) mode. The least-square method (LSM) for the statistically optimized inversion of multi-source data is used in LIRIC (Dubovik and King, 2000; Dubovik, 2004). The method requires covariance matrices of the lidar signal measurement errors as a function of the height z (Wagner et al., 2013). The lidar signal dispersion is calculated as a value for the measurement error at λ_i and z. Sixty thousand lidar signals collected over about 30 min to increase the signal-to-noise ratio are used in this study for each LIRIC run. Then, the standard deviation $\sigma_{\lambda i}(z)$ is calculated from LIRIC to estimate the dispersion and hence, the errors of the input lidar signals. The root mean square (RMS) value of the standard deviation $\sigma_{\lambda i}(z)$ taken all over the lidar signal altitude-range (RMS-$\sigma_{\lambda i}$) is calculated to obtain a mean column estimate of the dispersion of the input lidar signals at λ_i. The residuals $\rho_{\lambda i}(z)$ between the observed lidar signal values and the corresponding ones calculated from LIRIC are minimized to retrieve fine and coarse particle volume concentration profiles of good accuracy. To this end, the lidar input parameters z_o and z_f, and the regularization parameter sets are varied. We decided to calculate the root mean square value of the residuals taken all over the lidar signals altitude-range (RMS – $\rho_{\lambda i}$), to obtain a mean estimate of the LIRIC retrieval accuracy at each wavelength λ_i: the smaller is the RMS – $\rho_{\lambda i}$ value the higher is the retrieval accuracy. Hence, for each set of input lidar signals, several runs have been performed to minimize RMS – $\rho_{\lambda i}$ by varying realistic z_o, z_f, and regularization parameter values. Then, we have required that only the

AMTD
7, 8881–8926, 2014

LIRIC outputs satisfying the following condition

$$\mathrm{RMS} - \rho_{\lambda i} \leq 2 \times \mathrm{RMS} - \sigma_{\lambda i} \quad (1)$$

at 355, 532 and 1064 nm, respectively, could be considered of good-accuracy. More than 20 LIRIC outputs satisfying condition (1) have commonly been used in this study to calculate the mean fine $C_{\mathrm{f,\,a}}(\lambda_i, z)$ and coarse $C_{\mathrm{c,\,a}}(\lambda_i, z)$ particle volume concentration profiles. The $C_{\mathrm{f,\,a}}(\lambda_i, z)$ and $C_{\mathrm{c,\,a}}(\lambda_i, z)$ uncertainties have been set equal to ±1 standard deviation (SD) of the corresponding mean value. We know that we could use a different procedure than the above mentioned to calculate $C_{\mathrm{f,\,a}}(\lambda_i, z)$ and $C_{\mathrm{c,\,a}}(\lambda_i, z)$ mean values and corresponding standard deviations. However, we believe that the indicated one to go too well. Aerosol extinction and backscatter coefficients from LIRIC, $\beta_{\mathrm{L}}(\lambda_i, z)$ and $\alpha_{\mathrm{L}}(\lambda_i, \mathrm{z})$, respectively, are defined as

$$\alpha_{\mathrm{L}}(\lambda_i, z) = C_{\mathrm{f}}(\lambda_i, z) a_{\mathrm{f}}(\lambda_i) + C_{\mathrm{c}}(\lambda_i, z) a_{\mathrm{c}}(\lambda_i) \quad (2)$$

$$\beta_{\mathrm{L}}(\lambda, z) = C_{\mathrm{f}}(\lambda_i, z) b_{\mathrm{f}}(\lambda_i) + C_{\mathrm{c}}(\lambda_i, z) b_{\mathrm{c}}(\lambda_i) \quad (3)$$

For each set of lidar data, the mean extinction and backscatter profile is calculated by averaging all $\alpha_{\mathrm{L}}(\lambda_i, z)$ and $\beta_{\mathrm{L}}(\lambda_i, z)$ profiles, respectively obtained from the LIRIC outputs satisfying condition (1). $\alpha_{\mathrm{L}}(\lambda_i, z)$ and $\beta_{\mathrm{L}}(\lambda_i, z)$ uncertainties are set equal to ±1 SD of the corresponding mean value. The aerosol extinction-to-backscatter ratio (also referred to as the aerosol Lidar Ratio, LR) and the fine mode fraction η_{L} at different wavelengths are computed as follows:

$$\mathrm{LR}_{\mathrm{L}}(\lambda_i, z) = \alpha_{\mathrm{L}}(\lambda_i, z) / \beta_{\mathrm{L}}(\lambda_i, z) \quad (4)$$

$$\eta_{\mathrm{L}}(\lambda_i, z) = \alpha_{\mathrm{L,f}}(\lambda_i, z) / \alpha_{\mathrm{L}}(\lambda_i, z) \quad (5)$$

where

$$\alpha_{\mathrm{L,f}}(\lambda_i, z) = C_{\mathrm{f}}(\lambda_i, z) a_{\mathrm{f}}(\lambda_i) \quad (6)$$

AMTD
7, 8881–8926, 2014

Ångstrom exponent profiles for different wavelength pairs are computed in accordance with the following relationship:

$$\text{Å}_L(\lambda_1, \lambda_2, z) = -\{\ln[\alpha_L(\lambda_1, z)/\alpha_L(\lambda_2, z)]\}/[\ln(\lambda_1/\lambda_2)] \quad (7)$$

For each input data set, mean lidar ratio, fine mode fraction and Ångström exponent profiles are calculated by averaging the $LR_L(\lambda_i, z)$, $\eta_L(\lambda_i, z)$ and $\text{Å}_L(\lambda_1, \lambda_2, z)$ profiles determined by the LIRIC outputs satisfying condition (1). Uncertainties are set equal to ±1 SD of the corresponding mean values.

2.2 The 3-wavelength UNILE lidar system

The ground-based lidar system at the Mathematics and Physics Department of Universita' del Salento (Lecce, 40.33° N; 18.11° E), that is used in this study and is identified as UNILE (UNIversity of LEcce) lidar, operates within EARLINET since May 2000 (De Tomasi and Perrone, 2003). It is nowadays composed by a 30 Hz Nd:YAG laser operating at its fundamental wavelength, 1064 nm, and the second and third harmonic at 532 and 355 nm, respectively. The backscattered radiation collected by the primary mirror of the Newton telescope and collimated by a plane convex lens, is spectrally resolved by means of dichroic mirrors and interferential filters. Then, the 1064 nm signal is detected by an avalanche photodiode and an A/D transient recorder. The signal at 532 and 355 nm are detected by photomultipliers connected to transient recorders that have both a 12 bit A/D conversion and a photon counting (PC) capability. In this way the full dynamic range of the lidar signals can be monitored. Transient recorders integrate over 2000 laser shots that correspond to about 60 s. The lidar system is estimated to achieve full overlap between 0.5–1.0 km above the ground level (a.g.l.). The UNILE lidar system was designed to derive elastically backscattered lidar profiles at 355 nm, 532 nm and 1064 nm, respectively and the 355 nm-linear volume depolarization ratio ($\delta(z)$) profile during day time measurements.

AMTD
7, 8881–8926, 2014

2.3 Constrained iterative inversion procedure

Aerosol extinction and backscatter coefficient profiles from LIRIC are compared with the corresponding ones retrieved from a constrained iterative inversion (CII) procedure (Perrone et al., 2014) to investigate the potential of the LIRIC method, as mentioned in the introduction. The constrained iterative inversion procedure, whose main advantages and drawbacks are presented and discussed in Perrone et al. (2014), is based on the assumption that the lidar ratio is constant over the altitude. More specifically, it allows determining aerosol extinction ($\alpha(\lambda_i, z)$) and backscatter ($\beta(\lambda_i, z)$) coefficient profiles from 3-wavelength lidar measurements by using as boundary conditions: (1) the AOT of a selected altitude range and (2) the total backscatter coefficient β_T (due to molecules (β_M) and aerosol (β)) at a far-end reference height z_f, and (3) by assuming that the aerosol optical microphysical properties are constant from the ground up to $z = z_o$. Note that constrains (1)–(3) are also used by LIRIC and that the AOTs at the lidar wavelengths are retrieved from collocated in space and time AERONET measurements, as in LIRIC. The uncertainties of $\alpha(\lambda_i, z)$ and $\beta(\lambda_i, z)$ retrieved from the constrained iterative procedure include statistical uncertainties due to the presence of noise on the received lidar signals and systematic uncertainties as the ones due to the assumed molecular profile, the reference backscatter ratio value, and the total measured AOT. As in LIRIC, radiosonde measurements at the meteorological station of Brindisi (http://esrl.noaa.gov/raobs/) that is 40 km north-west of the monitoring site of this study are used to define the air density vertical profiles. Mean extinction and backscatter coefficient profiles at each lidar wavelength are calculated by averaging a few thousand profiles generated from the constrained iterative procedure by changing boundary conditions. The $\alpha(\lambda_i, z)$ and $\beta(\lambda_i, z)$ uncertainties are set equal to one standard deviation of the mean value, respectively. The vertical profiles of the Ångstrom exponents for different wavelength pairs are calculated in accordance with Eq. (5). The spectral curvature $\Delta\text{Å}(z)$ that is set equal to the difference

$$\Delta\text{Å}(z) = \text{Å}(355, 532, z) - \text{Å}(532, 1064, z) \quad (8)$$

AMTD
7, 8881–8926, 2014

is also calculated. Ångstrom exponent and $\Delta\text{Å}(z)$ profiles are calculated from each extinction profile at 355, 532, and 1064 nm generated by the implemented iterative procedure. The mean profile of $\text{Å}(\lambda_1, \lambda_2, z)$ and $\Delta\text{Å}(z)$ is then calculated and the $\text{Å}(\lambda_1, \lambda_2, z)$ and $\Delta\text{Å}(z)$ uncertainties are set equal to one standard deviation of the corresponding mean values.

As mentioned, main boundary conditions used in the constrained iterative procedure are common to LIRIC. However, the constrained iterative procedure searches for height-independent lidar ratio (LR) values to satisfy the boundary conditions. By contrast, LIRIC uses a typical algorithm for solving inverse problems and searches for concentration profiles of aerosol modes invariant over the altitude that best match the AERONET column-integrated fine- and coarse-mode particle volume concentrations and the measured lidar data. As a consequence, aerosol extinction and backscatter coefficient profiles from LIRIC may differ from the corresponding ones retrieved from the constrained iterative procedure if the modal radii of the aerosol size distribution vary with z, as it will be shown in the following.

2.4 Graphical framework for the aerosol classification

The aerosol classification framework presented and discussed in Perrone et al. (2014) is used in this study to investigate the potential of LIRIC to retrieve vertical profiles of fine- and coarse-mode particle volume concentrations. The graphical classification framework allows to obtain an estimate of the dependence on altitude of the aerosol fine modal radius ($R_{\text{f,GF}}$) and of the fine mode contribution (η_{GF}) to the aerosol optical thickness at 532 nm from the spectral curvature $\Delta\text{Å}(z)$ vs. the Ångstrom exponent $\text{Å}(355, 1064, z)$ plot. Ångstrom exponents and spectral curvature are calculated from extinction coefficient profiles retrieved at 355, 532, and 1064 nm, in accordance with Eqs. (7) and (8). Figure 1 (black lines) shows the aerosol classification framework calculated by setting the real and imaginary refractive index value at 532 nm equal to 1.455 and 0.0047, respectively. The used n and k values are considered

AMTD
7, 8881–8926, 2014

representative of mixed aerosol types, in accordance with the discussion reported in Perrone et al. (2014). Mie calculations of the aerosol spectral extinction for selected fine ($R_{f,GF}$ = 0.02, 0.05, 0.1, 0.15, 0.2, 0.3, and 0.4 µm) and coarse ($R_{c,GF}$ = 0.5, 0.6, 0.7, and 0.8 µm) modal radii, combined in order to provide η_{GF} fractions at 532 nm of 1, 10, 30, 50, 70, 90, 99 %, have been performed to calculate the solid and dashed black lines of Fig. 1, which represent the graphical framework denoted as Mixed aerosol framework. Yellow solid and dashed lines in Fig. 1 represent the aerosol classification framework calculated by using the real and imaginary refractive index values for dust recently reported by Wagner et al. (2012), which are n = 1.55 and k = 0.008 at 532 nm. It is denoted as Dust framework and allows to highlight the sensitivity of the graphical framework to refractive index values. The dust refractive indices were calculated from laboratory measurements on dust samples (Wagner et al., 2012). The test shows that the average change in all the 49 grid points is of about 5 %. The sensitivity of the aerosol classification framework to changes in the coarse modal radii is revealed by the blue graphical framework of Fig. 1 (Dust rev. coarse). It was obtained by increasing of 50 % the coarse modal radii ($R_{c,GF}$ = 0.75, 0.9, 1.05, and 1.2 µm) and by using the real and imaginary refractive index values for dust from Wagner et al. (2012). The test shows that the graphical framework moves on average downward as the coarse modal radii are increased of 50 %. The average change in all the 49 grid points with respect to the Mixed aerosol framework (Fig. 1, black lines) is of about 4 %. Effects of refractive index and coarse modal radius changes have also been discussed in Gobbi et al. (2007). The Dust rev. coarse framework (Fig. 1, blue lines) is best suited for aerosol loads heavily affected by dust particles.

3 Results

Three case studies are analyzed in this section to investigate the potential of LIRIC to retrieve vertical profiles of fine and coarse-mode particles under different aerosol load scenarios. More specifically, one case deals with aerosol measurements affected

AMTD
7, 8881–8926, 2014

by anthropogenic, biomass-burning, and soil particles. The second case deals with anthropogenic pollution affected by marine aerosol and the last one deals with aerosols significantly affected by Sahara dust.

3.1 Case study: 29 August 2011

Results on lidar measurements performed on 29 August 2011 from 13:56 to 14:27 UTC are first discussed in this section. Figure 2a shows the vertical profiles of the mean fine $C_{\mathrm{f,\,a}}(\lambda_i, z)$ (black dotted line) and coarse $C_{\mathrm{c,\,a}}(\lambda_i, z)$ (pink dotted line) particle volume concentration with corresponding uncertainties (error bars) retrieved from LIRIC, in accordance with the methodology described in Sect. 2.1. AERONET inversion products retrieved from sun/sky photometer measurements (Lecce University) performed at 14:12 UTC have been used by LIRIC. Figure 2a shows that fine and coarse particle volume concentrations are of the same order of magnitude and vary similarly with the altitude. Atmospheric particle sizes on average vary with source type and/or the pathways they have followed before reaching the monitoring site. So, Fig. 2a indicates that particles from different sources and/or from different pathways have contributed to the aerosol load and that the different contributions occurred almost at all altitudes sounded with the lidar. We remind here that different aerosol types can be monitored at the monitoring site of this study, because of its geographical location in the Central Mediterranean. In fact, south eastern Italy may be affected by polluted particles from urban and industrial areas of west, north, and east Europe, marine aerosols from the Mediterranean itself and/or transported from the Atlantic, biomass burning particles, often produced in forest fire, mainly during summer, and dust particles from the Sahara desert and the arid regions in the Iberian Peninsula (Tafuro et al., 2007). Figure 3a shows the pathways estimated at 14:00 UTC of the ten day analytical backtrajectories with arrival heights at 1, 2, and 3 km above the ground level (a.g.l.), calculated from the Hybrid Single Particle Lagrangian Integrated Trajectory Model (HYSPLIT) (Draxler and Rolph, 2003). Advection patterns similar to the one of Fig. 3a are rather frequent over southeastern Italy mainly in summer (Perrone et al., 2013). The time evolution of

AMTD
7, 8881–8926, 2014

the altitude of each backtrajectory is plotted in Fig. 3b. Figure 3a reveals that the air masses reached southeastern Italy after crossing several populated regions of west, north, and east Europe. More specifically, Fig. 3b shows that the 1 km-arrival-height air masses travelled close to the ground level 2–3 days before their arrival time, and that the 2 km-arrival-height air masses travelled close to the ground level over southeastern Spain and several eastern Europe regions. As a consequence, they were likely responsible for the lifting at high altitudes of soil and local anthropogenic particles. The ground surface heating, generating turbulent fluxes mainly in summer also favors the lifting of ground particles and the mixing with particles located at higher altitudes. Moreover, the lack of rainy days mainly occurring in summer over southern Europe enhances the natural and anthropogenic soil resuspension. In fact, some of the authors found that both the aerosol load and the maximum altitude where aerosols are located increase from winter to summer (De Tomasi et al., 2006). Figure 3c shows that the 10 day fire map by MODIS from 20 to 29 August 2011 (https://firms.modaps.eosdis.nasa.gov/firemap/) and we observe that the air masses overpassed biomass burning areas (identified as yellow-dots in Fig. 3c) where they were likely enriched by biomass burning aerosols prior to the observation. Therefore, the fine and coarse mode volume concentrations (Fig. 2a) are likely due to anthropogenic pollution and biomass burning particles, and resuspended soil and sea-salt particles, respectively. Dotted lines in Fig. 2b–d show the vertical profiles of $\alpha_L(\lambda_i, z)$, $LR_L(\lambda_i, z)$, and $\eta_L(\lambda_i, z)$, respectively with corresponding uncertainties retrieved from LIRIC in accordance with Eqs. (2)–(5). The large extinction coefficient values at 355 nm and the strong dependence of $\alpha_L(\lambda_i, z)$ on λ_i indicate that fine mode particles were dominant, since the efficiency of scattering by small particles is more pronounced at the short wavelengths (Lopatin et al., 2013). The high LR values at 355 nm which span the the 79–84 sr range from the ground up to 3.9 km a.g.l. (Fig. 2c, blue dotted line), also indicate that the aerosol load was affected by a significant contribution of fine absorbing particles, like anthropogenic and biomass burning particles (e.g. Barnaba et al., 2007; Mamouri et al., 2012 and references therein). LR values at 532 and 1064 nm are ≅ 54 and 30 sr, respectively. It is worth noting that

AMTD
7, 8881–8926, 2014

recent numerical results from Lopatin et al. (2013) have revealed that the LR dependence on λ_i for fine mode absorbing particles is rather close to the one revealed by Fig. 2c (dotted lines). $\eta_L(355, z)$ mean values which span the 0.86–0.94 range from the ground up to 3.9 km a.g.l. furthermore show that the 355 nm-extinction is mainly determined by fine mode particles. η_L spans the 0.72–0.86 and the 0.30–0.52 range at 532 and 1064 nm, respectively (Fig. 2d), since the extinction by fine mode particles decreases with the wavelength increase. Ångstrom exponent profiles with corresponding uncertainties for different wavelength pairs are plotted in Fig. 4a and b (dotted lines) and we observe that they are on average characterized by values larger than 1 from the ground up to 3.9 km a.g.l. for all tested wavelength pairs, as expected when fine mode particles are dominant. However, one must be aware that large fine mode particles can have the same Ångstrom exponent of mixtures of coarse and small fine mode particles, as Schuster et al. (2006) have clearly shown in Fig. 3 of their paper. The spectral difference $\Delta\text{Å}_L(z)$ can allow inferring the occurrence of bimodal aerosol size distribution, according to Schuster et al. (2006). Figure 4b (red dotted line) shows the vertical profile of $\Delta\text{Å}_L(z)$ mean values with corresponding uncertainties: mean values which span the 0.02–0.32 range from the ground up to 3.9 km a.g.l., indicate that the aerosol size distribution is made by two separate modes with a significant coarse mode contribution (e.g. O'Neill et al., 2003; Schuster et al., 2006 and references therein).

Aerosol extinction coefficient ($\alpha(\lambda_i, z)$) and lidar ratio ($\text{LR}(\lambda_i, z)$) profiles retrieved from the constrained iterative inversion procedure by using the lidar data set used in LIRIC, are plotted in Fig. 2b and c (solid lines), respectively to investigate the LIRIC ability to retrieve vertical profiles of aerosol optical parameters. Figure 2b reveals that the differences between the LIRIC (dotted line) and the CII-procedure (solid lines) extinction coefficients vary with altitude and wavelength and decrease with the increase of λ_i. More specifically, Fig. 2b shows that α (355 nm, z) values are smaller than corresponding α_L(355 nm, z) values within 1–2 km a.g.l. The extinction coefficient sensitivity to fine mode particles is large at 355 nm. Therefore, the vertical profile of the fine-mode size distribution retrieved from LIRIC (Fig. 2a, black dotted) is likely responsible for the

AMTD
7, 8881–8926, 2014

above mentioned differences. Note that the differences between α (355 nm, z) and α_L(355 nm, z) on average decrease with the altitude increase. Lidar ratios from the CII procedure (Fig. 2c, solid lines) are in good accordance within ±1 SD of mean values with corresponding values from LIRIC (Fig. 2c, dotted lines). It is also worth noting that the uncertainties associated with the CII procedure LR values are larger than the variability range of corresponding LR_L values, since they vary weakly with the altitude. Note that Wagner et al. (2013) also found that LR_L values were characterized by a rather weak dependence on z. Hence, the differences between the LIRIC and the CII procedure aerosol extinction profiles revealed by Fig. 2b are not likely due to the assumption of height-independent lidar ratios by the CII procedure. Figure 4a and b shows by solid lines the Ångstrom exponent profiles (Å(λ_1, λ_2, z)) with corresponding uncertainties retrieved from the CII procedure for different wavelength pairs. We remind here that Ångstrom exponents are good indicators of the dominant aerosol size (Schuster et al., 2006 and references therein). As a consequence, the Å(λ_1, λ_2, z) changes with z are linked to the changes with z of the aerosol size distribution. Figure 4a shows that Å(355, 532, z) values (blue solid line) are smaller than the corresponding $Å_L$(355, 532, z) values (blue dotted line) up to ∼ 2 km a.g.l. and take larger values at z > 2.8 km a.g.l. By contrast, Fig. 4b reveals that Å(355, 1064, z) values are in reasonable accordance with the corresponding $Å_L$(355, 1064, z) values up to ∼ 3.9 km a.g.l. The Ångstrom sensitivity to particle size which varies with the wavelength pair is responsible for these results. Å values calculated from shorter wavelength pairs (e.g. λ = 355, 532 µm) are sensitive to the fine mode effective radius but not the fine mode fraction, according to Schuster et al. (2006). Conversely, Å values calculated from longer wavelength pairs (e.g. λ = 532, 1064 µm) are sensitive to the fine mode fraction of aerosols but not the fine mode radius. In fact, Schuster et al. (2006) pointed out that it is important to consider the wavelength pair used to calculate the Ångstrom exponent when making qualitative assessments about the corresponding aerosol size distribution. Note that the increase of Å(355, 532, z) with z (Fig. 4a, solid line) is due to the increase with z of the α (355, z)/α (532, z) ratio (Eq. 7). Therefore, the dependence of Å(355, 532, z) on z

AMTD
7, 8881–8926, 2014

may indicate that the modal radius of the fine mode particles decreases with the altitude increase. The Ångstrom exponent spectral difference from LIRIC $\Delta\mathring{A}_L(z)$ (Fig. 4b, red dotted line) varies weakly with z with respect to $\Delta\mathring{A}(z)$ (Fig. 4c, red solid line), which takes negative values from the ground up to ∼ 2 km a.g.l. and positive values at $z > 2.7$ km a.g.l. More specifically, Fig. 4b (solid red line) shows that $\Delta\mathring{A}(z)$ on average increases with z. The increase with z of the fine mode particle contribution is likely responsible for this result, in accordance with Eq. (8). In conclusion, the comparison of Angstrom exponent and spectral difference profiles from LIRIC and the CII-procedure has revealed some marked differences which have likely been determined by the LIRIC assumption that aerosol modal radii are invariant over the altitude. Calculated $\Delta\mathring{A}_L(z)$ vs. $\mathring{A}_L(355, 1064, z)$ values within 1–3.9 km a.g.l. are plotted on the graphical framework of Fig. 5 (open triangles) to investigate to what extent, the estimates of the fine mode radius ($R_{f,GF}$) and of the fine mode fraction (η_{GF}) from the graphical framework (Sect. 2.4) are in accordance with corresponding LIRIC results. The triangle size in Fig. 5 accounts for the $\Delta\mathring{A}_L(z)$ and $\mathring{A}_L(355, 1064, z)$ uncertainties. Different colors are used to represent $\Delta\mathring{A}_L(z)$ vs. $\mathring{A}_L(355, 1064, z)$ values referring to different z, as indicated by the color bar on the rigth of Fig. 5. Data at $z \leq 1$ km have not been plotted since they are likely affected by the lidar field of view: the lidar system is estimated to achieve full overlap at $z \geq 1$ km a.g.l. (Sect. 2.2). The graphical framework calculated for $n = 1.455$ and $k = 0.0047$ at 532 nm (Mixed aerosol framework) is shown in Fig. 5. These refractive index values are considered representative of aerosol loads affected by mixed aerosol types, in accordance with the discussion reported in Perrone et al. (2014). It is interesting to observe: (1) that the $\Delta\mathring{A}_L(z)$ vs. $\mathring{A}_L$ (355, 1064, z) values are on the framework area delimited by η_{GF} values spanning the ∼ 70–80 % range, in good accordance with the $\eta_L(532, z)$ values of Fig. 2d (green dotted line) and (2) that all data points are located on the $R_{f,GF} \cong 0.09$ µm curve, in satisfactory accordance with the columnar averaged aerosol fine modal radius retrieved from AERONET which is $R_{f,A} = 0.085$ µm. The fine modal radius is calculated from the value of the AERONET fine volume median radius $R_{Vf,A}$ (µm) by the following relationship (Seinfeld and Pandis,

AMTD
7, 8881–8926, 2014

1998):

$$\ln R_{f,A} = \ln R_{Vf,A} - 3\ln^2 \sigma_g \quad (9)$$

where σ_g represents the geometric standard deviations for fine mode particle, that is an AERONET aerosol product. Note that these results reveal the feasibility of the graphical framework to provide a good estimate of the fine mode fraction and the fine modal radius retrieved from LIRIC. Full dots and error bars in Fig. 5 show for comparison ΔÅ(z) vs. Å(355, 1064, z) mean values with corresponding standard deviations. It is interesting to observe: (1) that the ΔÅ(z) vs. Å(355, 1064, z) mean values are on the graphical framework area delimited by η_{GF} values spanning the 70–99 % range, in satisfactory accordance with LIRIC results, and (2) that the particle fine modal radius varies with z spanning the ∼ 0.02–0.17 µm range, in contrast to LIRIC results (triangle). Note that the CII-procedure does not make any constrain on the dependence on altitude of the particle size. The selection of a height-independent LR to match the AOT represents the main source of uncertainties of the CII-procedure, according to Perrone et al. (2014). Therefore, if we assume that the graphical framework can provide a reliable estimate of the fine particle modal radius, the ΔÅ(z) vs. Å(355, 1064, z) scatter plot (Fig. 5, full dots) shows that the fine particle modal radius decreases with the altitude increase. Figure 5 also shows that the value of $R_{f,GF} \cong 0.09$ µm retrieved from LIRIC locates on the middle of variability range of the fine particle modal radii retrieved from the ΔÅ(z) vs. Å(355, 1064, z) plot. Backtrajectory pathways (Fig. 3a and b) and the MODIS fire map (Fig. 3c), which have indicated that aerosol from different sources have contributed to the aerosol load monitored by the lidar on 29 August 2011, can support the dependence on z of the fine modal radius revealed by Fig. 5 (full dots). The gravitational settling of large fine mode particles has likely contributed to the decrease of the fine modal radius with the altitude increase revealed by Fig. 5 (full dots). Note that the lack of rainy days occurring on summer over the central Mediterranean favors the aging of aerosol and likely the gravitational settling of large fine mode particles. Moreover, the large solar flux on summer time favors the formation of new anthropogenic particles

AMTD
7, 8881–8926, 2014

by photochemical reactions (Seinfeld and Pandis, 1998). Note that the fine modal radius estimates retrieved from the $\Delta\text{Å}(z)$ vs. $\text{Å}(355, 1064, z)$ scatter plot (Fig. 5, full dots) can allow understanding the differences between $\alpha_L(355\,\text{nm}, z)$ and α (355 nm, z) revealed by Fig. 2b (blue lines) within 1–2 km a.g.l. In fact, the large values of the fine modal radius within 1–2 km a.g.l. (Fig. 5, full dots) have likely been responsible for the smaller α (355 nm, z) values with respect to the $\alpha_L(355\,\text{nm})$ values. In conclusion, the above comments may lead to infer that the search of height-independent aerosol fine and coarse modal radii can represents the main source of uncertainties of the LIRIC aerosol products and hence, the main limit of the LIRIC method. Terefore, the uncertainties of the LIRIC aerosol products may be significant mainly when aerosols from different sources and hence, characterized by different size distributions, affect the whole aerosol load, as commonly occurs over the Central Mediterranean (e.g. Perrone et al., 2014).

3.2 Case study: 12 September 2011

Figure 6a shows the vertical profiles of the mean fine $C_{f,a}(\lambda_i, z)$ and coarse $C_{c,a}(\lambda_i, z)$ particle volume concentration with corresponding standard deviations (error bars), retrieved from LIRIC by combining lidar measurements performed on 12 September 2011 from 14:06 to 14:36 UTC and AERONET inversion products, retrieved from sun/sky photometer measurements (Lecce University) performed at 14:21 UTC. Fine and coarse particle volume concentrations vary similarly with the altitude but, fine particle volume concentrations are nearly 1.5 larger than coarse particle volume concentrations. Note that previous analyses of the Lecce University-AERONET inversion products have revealed that the columnar aerosol volume size distribution is on average bimodal and that fine mode particles are dominant during all year (Tafuro et al., 2007; Bergamo et al., 2008). The bimodal structure of the size distribution spectrum indicates that along with fine mode particles, which are mainly of anthropogenic origin, coarse mode particles as those of natural (marine and crustal) origin, also contribute to the aerosol load during all year. Dotted lines in Fig. 6b–d shows the vertical profiles of

AMTD
7, 8881–8926, 2014

$\alpha_L(\lambda_i, z)$, $LR_L(\lambda_i, z)$, and $\eta_L(\lambda_i, z)$, respectively with corresponding uncertainties calculated in accordance with the methodology outlined in Sect. 2.1. The extinction coefficient profiles indicate that a vertically homogeneous layering of aerosol particles was detected from the lidar from the ground up to ~ 3 km a.g.l. Lidar ratio values that vary rather weakly with z, are equal to about 25, 60 and 75 sr at 1064, 532, and 355 nm, respectively. These values have likely been determined by the significant contribution of fine absorbing particles (Lopatin et al., 2013). $\eta_L(355, z)$, $\eta_L(532, z)$, and $\eta_L(1064, z)$ mean values span the 0.95–0.99, 0.90–0.99, and 0.60–0.95 range, respectively from the ground up to ~ 4.2 km a.g.l. The Ångstrom exponent vertical profiles for different wavelength pairs are plotted in Fig. 7a and b (dotted lines). They take values > 1.5 for all tested wavelength pairs up to ~ 3 km a.g.l. as it occurs when fine mode particles are dominant. The pathways of the seven day HYSPLIT backtrajectories with arrival heights at 0.5, 1.5, and 2.5 km a.g.l. (Fig. 8a and b) at 14:00 UTC of 12 September 2011, can support the aerosol properties revealed by Figs. 6 and 7. Figure 8a shows that the 0.5 km air masses crossed the Tyrrhenian Sea at quite low altitudes before reaching southern Italy and as a consequence they have likely been responsible for the advection of sea-salt particles. By contrast, the 1.5 and 2.5 km air masses which have their origin over the Atlantic Sea at high altitudes are characterized by a similar pathway and reached Southeastern Italy after crossing Central Europe and the eastern coast of the Adriatic Sea. Therefore, they have mainly been responsible for the advection of anthropogenic pollution and sea-salt particles lifted up to ~ 3 km a.g.l. Solid lines in Fig. 6b and c shows the aerosol extinction coefficient and lidar ratio profiles retrieved from the constrained iterative inversion procedure. The differences between the CII-procedure (solid lines) and the LIRIC (dotted line) extinction coefficients vary with altitude and wavelength and decrease with the increase of λ_i. More specifically, they are within ±1 SD of mean values at 1064 nm, while α (355 nm, z) values are ~ 1.1 times larger than the corresponding α_L (355 nm, z) values from the ground up to ~ 1.9 km a.g.l. Lidar ratios (Fig. 6c) from the CII-procedure are in accordance within ±1 SD of mean values with corresponding values from LIRIC, which show a rather weak dependence

AMTD
7, 8881–8926, 2014

on z, as mentioned. Ångstrom exponent profiles from the CII procedure also are in reasonable accordance with the corresponding profiles from LIRIC, within ±1 SD of mean values and up to ∼ 3 km a.g.l. Both the LIRIC and the CII aerosol parameters indicates that the aerosol microphysical properties were characterized by a weak dependence on altitude on the afternoon of 12 September. This result may be due to the fact that the 1.5 and 2.5 km air masses have followed the same pathway before reaching southern Italy and as a consequence, they have likely been responsible for the advection of particles with similar optical and microphysical properties within ∼ 1–3 km a.g.l. Open triangles in Fig. 9 show $\Delta\text{Å}_L(z)$ vs. $\text{Å}_L(355, 1064, z)$ within 1–3 km a.g.l. $\Delta\text{Å}_L(z)$ vs. $\text{Å}_L(355, 1064, z)$ values are on the framework area delimited by η_{GF} values spanning the ∼ 85–95 % range, in reasonable accordance with the $\eta_L(532, z)$ values of Fig. 2d (green dotted line) and are located on the $R_{f,GF} \cong 0.09$ µm curve. This value is in satisfactory accordance with the columnar averaged aerosol fine modal radius retrieved from AERONET which is $R_{f,A} = 0.082$ µm. Note that the $\Delta\text{Å}_L(z)$ vs. $\text{Å}_L(355, 1064, z)$ plot shows ones more the feasibility of the graphical framework to provide a good estimate of the fine mode fraction and the fine modal radius retrieved from LIRIC. Full dots in Fig. 9 show the scatterplot of $\Delta\text{Å}(z)$ vs. $\text{Å}(355, 1064, z)$ with corresponding uncertainties (error bars) within 1–3 km a.g.l. Different colors are used to represent values referring to different z, as indicated by the color bar on the right of Fig. 9. $\Delta\text{Å}(z)$ vs. $\text{Å}(355, 1064, z)$ mean values are on the graphical framework area delimited by η_{GF} and $R_{f,GF}$ values spanning the 90–99 % and the 0.08–0.10 µm range, in satisfactory accordance with the corresponding parameters from LIRIC. Hence, Fig. 9 reveals that the aerosol products from LIRIC are in satisfactory accordance with the corresponding ones from the CII procedure, when the particle fine modal radius varies weakly with the altitude.

3.3 Case study: 6 August 2012

The last case study deals with lidar measurements performed on 6 August 2012. Aerosol affected by Sahara dust particles were monitored on 6 August, as shown in

AMTD
7, 8881–8926, 2014

the following. Figure 10 (black line) shows the vertical profile of the linear particle depolarization-ratio (δ_p (z)) with corresponding uncertainties (Perrone et al., 2014), calculated from lidar measurements at 355 nm performed on 6 August 2012 from 14:57 to 15:21 UTC. The δ_p (z) mean values that are $\cong$ 20 % within 2–5 km a.g.l. show the altitude range affected by non spherical particles. Then, analytical backtrajectories and the BSC-DREAM model indicate that the δ_p (z) values were determined by the advection of Sahara dust particles. Figure 11 shows the pathways estimated at 15:00 UTC of 6 August 2012, of the 10 day HYSPLIT backtrajectories with arrival heights at 1, 2.5, and 4.5 km a.g.l. We observe that the 2.5 km air masses crossed northern Morocco at very low altitudes (Fig. 11b) and that the 4.5 km air masses crossed central Algeria and Morocco at very low altitudes (Fig. 11b) before reaching southeastern Italy. So, they have likely been responsible for the advection of Sahara dust particles lifted from the ground up $\sim$ 5 km a.g.l. The 1 km air masses have their origin over the Atlantic and travelled at high altitudes before reaching southern Italy. The advection of Sahara dust particles over southern Italy occurred from midday of 4 August up to the night of 9 August, in accordance with the BSC-DREAM simulations (http://www.bsc.es/earth-sciences/mineral-dust-forecast-system/bsc-dream8b-forecast/north-africa-europe-and-middle-ea-0). The red line in Fig. 10 shows the vertical profile of the dust particle concentration simulated from the BSC-DREAM for the monitoring site of this study, at 12:00 UTC of 6 August. Figure 10 (red line) reveals the existence of a dust layer extending from the ground up to $\sim$ 5 km a.g.l., with mass concentrations larger than 70 $\mu g\,m^{-3}$ at $\sim$ 2 km a.g.l. Note that the dust concentration profile of Fig. 10 (red line) supports the δ_p (z) profile (Fig. 10, black line) retrieved from lidar measurements. It is also worth noting that during the Saharan Mineral Dust Experiment campaigns, dust depolarization ratios were around 0.23–0.25 at 355 nm (Wagner et al., 2013), in satisfactory accordance with the results of this study (Fig. 10, black line). Figure 12a shows the mean fine $C_{f,a}(\lambda_i, z)$ and coarse $C_{c,a}(\lambda_i, z)$ particle volume concentration profiles with corresponding $\pm$1 SD of mean values (error bars). They have been retrieved from LIRIC by combining lidar measurements

AMTD
7, 8881–8926, 2014

performed on 6 August 2012 from 14:57 to 15:21 UTC and AERONET inversion products from sun/sky photometer measurements (Lecce University) performed at 15:13 UTC. Coarse particle volume concentrations are dominant up to ∼ 5 km a.g.l. in satisfactory accordance with particle depolarization ratio measurements, dust particle concentration from the BSC-DREAM (Fig. 10) and backtrajectory pathways (Fig. 11). Dotted lines in Fig. 12b show the LIRIC extinction coefficient vertical profiles at 355, 532 and 1064 nm with the corresponding ±1 SD of mean values (error bars). A vertically inhomogeneous layering of aerosol particles was detected by the lidar within 1–7 km a.g.l. The detected aerosol layering may be supported by the vertical structure of the potential temperature (θ) and relative humidity (RH) profiles (Fig. 13), which have been retrieved from radiosonde measurements performed at the meteorological station of Brindisi (http://esrl.noaa.gov/raobs/) on 6 August at 11:00 UTC. Figure 13 (full dots) reveals that the potential temperature increases with altitude and shows a temperature inversion at about 0.5, 1.8, and 5 km a.g.l. The RH profile (Fig. 13 open dots) is also quite dependent on altitude. RH takes rather small values (10–20 %) within 1–3.2 km a.g.l. and then increases with z reaching the value of 60 % at ∼ 4.8 km a.g.l. These results indicate that rather dry particles were located within 1–3.2 km a.g.l. Dotted lines in Fig. 12c and d shows the vertical profiles of $LR_L(\lambda_i, z)$ and $\eta_L(\lambda_i, z)$, respectively with corresponding ±1 SD of mean values (error bars). Lidar ratio values span the 84–71 sr, 61–56 sr, and 51–47 sr range at 355, 532, and 1064 nm, respectively and decrease slowly with z. The fine mode fractions increase with z spanning the 0.10–0.88, 0.06–0.74, and 0.02–0.40 range at 355, 532, and 1064 nm, respectively, from the ground up to ∼ 5.4 km a.g.l. Solid lines in Fig. 12b and c show the aerosol extinction coefficient and lidar ratio profiles, respectively retrieved from the constrained iterative inversion procedure. The differences between the CII-procedure (solid lines) and the LIRIC (dotted line) extinction coefficients vary significantly both with the altitude and the lidar wavelength (Fig. 12b). Mean lidar ratios from the CII-procedure that are equal to 64 ± 10, 56 ± 8 and 47 ± 18 sr at 355, 532, and 1064 nm, respectively, are typical of Sahara dust particles, in accordance with previous studies (e.g. Wagner et al.,

AMTD
7, 8881–8926, 2014

2013; Perrone et al., 2014, and references therein). The lidar ratio values from the CII procedure at 1064 nm and 532 nm are in good accordance within ±1 SD of mean values, with the corresponding values from LIRIC. By contrast, the $LR_L(355, z)$ values are larger than the corresponding LR(355, z) values from the ground up to ∼ 5.4 km a.g.l. Dotted and solid lines in Fig. 14a and b show the Ångstrom exponents for different wavelength pairs retrieved from LIRIC and the CII-procedure extinction coefficient, respectively up to 5.4 km a.g.l. The differences between $Å_L$ and corresponding Å values vary significantly with altitude and wavelength pairs. In fact, $Å_L$ (532, 1064, z) and corresponding Å(532, 1064, z) values are in satisfactory accordance within ±1 SD from 1.5 up 5.4 km a.g.l. By contrast, the Å(355, 532, z) values are smaller than the corresponding $Å_L(355, 532, z)$ values within 2.5–4.5 km a.g.l. Red solid and dotted lines in Fig. 14b show the vertical profile of the spectral curvature from the CII-procedure and LIRIC, respectively. ΔÅ(z) values vary from about −1 up to 1 within 1.0–5.4 km a.g.l. By contrast, the $\Delta Å_L(z)$ values are close to zero within the same altitude range. Open triangles in Fig. 15 show $\Delta Å_L(z)$ vs. $Å_L(355, 1064, z)$ from 1 up to 5.4 km a.g.l. Different colors represent $\Delta Å_L$ vs. $Å_L$ values referring to different z, as indicated by the color bar on the right of Fig. 15. The triangle size accounts for the $\Delta Å_L(z)$ and $Å_L(355, 1064, z)$ uncertainties. The blue solid and dashed lines of Fig. 15 represent the Dust rev. coarse graphical framework, since it is considered best suited for aerosol loads heavily affected by desert dust particles, in accordance with the discussion of Sect. 2.4. $\Delta Å_L$ vs. $Å_L$ mean values are on the graphical framework area delimited by η_{GF} values varying up to ∼ 70 % in good accordance with the $\eta_L(532\,nm, z)$ variability range (Fig. 12d), and are mainly located on the $R_{f,GF} \cong 0.1$ µm solid line, since the LIRIC method does not allow to the fine modal radius to change with z. Note that the columnar averaged aerosol fine modal radius from AERONET is $R_{f,A} = 0.041$ µm. The rather low $R_{f,A}$ value retrieved from AERONET is likely due to the fact that the Dubovik inversion procedure overestimates the fine mode fraction for dust-dominated aerosol conditions, according to Kleidman et al. (2005). We believe that the $\Delta Å_L$ vs. $Å_L$ plot shows once again that the graphical framework can provide a reliable estimate of the particle fine mode

AMTD
7, 8881–8926, 2014

fraction and of the fine particle modal radius retrieved from LIRIC. Full dots and error bars in Fig. 15 show $\Delta\text{Å}(z)$ vs. Å(355, 1064, z) with corresponding uncertainties within 1–5.4 km a.g.l. ΔÅ vs. Å mean values are on the graphical framework area delimited by η_{GF} values varying up to ~ 70 % (in good accordance with LIRIC results) and $R_{f,GF}$ values spanning the 0.02–0.3 µm range. The main differences between the $\Delta\text{Å}_L$ (z) vs. Å_L(355, 1064, z) and the $\Delta\text{Å}(z)$ vs. Å(355, 1064, z) plot are due to the fact that the $\Delta\text{Å}(z)$ vs. Å(355, 1064, z) data points show that the fine modal radius vary with the altitude range. This result can be supported by the backtrajectory pathways of Fig, 11 which vary with the arrival height. It is well known that the optical and microphysical properties of advected particles are quite dependent on both the source regions and the pathways they have followed before reaching the monitoring site. The $\Delta\text{Å}(z)$ vs. Å(355, 1064, z) plot indicates that the data points within ~ 1–2.2 km a.g.l. are on the graphical framework area delimited by $R_{f,GF}$ values spanning the 0.02–0.15 µm range. By contrast, the $\Delta\text{Å}(z)$ vs. Å(355, 1064, z) mean values within ~ 2.2–4.8 km a.g.l. are on the graphical framework area delimited by $R_{f,GF}$ values spanning the 0.1–0.3 µm range. The depolarization lidar measurements, the BSC-DREAM dust concentration profile, and backtrajectory pathways support last results, since they indicate that the contribution of Sahara dust particles was greater within 2–5 km a.g.l. It is also worth noting that the $R_{f,GF} \cong 0.1$ µm value retrieved from the $\Delta\text{Å}_L(z)$ vs. Å_L(355, 1064, z) plot is located within the $R_{f,GF}$ variability range ($\cong$ 0.02–0.3 µm) retrieved from the $\Delta\text{Å}(z)$ vs. Å(355, 1064, z) plot. Finally, it is worth mentioning that the dependence on z of the fine modal radius estimates from the $\Delta\text{Å}(z)$ vs. Å(355, 1064, z) plot, can allow understanding the differences between $\alpha_L(\lambda_i, z)$ and $\alpha(\lambda_i, z)$ revealed by Fig. 12b. In fact, the larger values of the fine modal radius estimates from the $\Delta\text{Å}(z)$ vs. Å(355, 1064, z) plot are likely responsible for the smaller values of $\alpha(\lambda_i, z)$ within ~ 2.5–4.8 km a.g.l. (Fig. 12b), with respect to the corresponding $\alpha_L(\lambda_i, z)$ values. Hence, the analysis of this last case study has once again indicated that the differences between the aerosol products from LIRIC and the CII procedure can be quite large when the fine modal radius and hence the aerosol size distribution vary with the altitude.

AMTD
7, 8881–8926, 2014

4 Summary and conclusion

The potential of LIRIC to retrieve the vertical profiles of fine- and coarse-mode particle volume concentrations by combining AERONET sun/sky photometer aerosol products and 3-wavelength elastic lidar signals, has been investigated. An aerosol classification framework, which allows estimating the dependence on altitude of the aerosol fine modal radius and of the fine mode fraction from the Ångstrom exponent spectral difference (ΔÅ) vs. the 355–1064 nm-Ångstrom exponent plot, has been used to investigate the potential of LIRIC to retrieve the vertical profiles of fine- and coarse-mode particle volume concentrations. The LIRIC ability to retrieve the vertical profiles of aerosol extinction coefficients ($\alpha_L(\lambda_i, z)$), lidar ratios ($LR_L(\lambda_i, z)$), Angstrom exponents ($Å_L(\lambda_1, \lambda_2, z)$) for different wavelength pairs, and of the spectral difference ($\Delta Å_L$), has been investigated by comparing LIRIC results with the corresponding ones from a constrained iterative inversion procedure. The CII-procedure that is based on the assumption of a lidar ratio constant over the altitude, allows retrieving aerosol extinction coefficient $\alpha(\lambda_i, z)$ and lidar ratio $LR(\lambda_i, z)$ profiles from 3-wavelength lidar measurements by using as boundary conditions: (1) the AOT of a selected altitude range and (2), the total backscatter coefficient β_T (due to molecules (β_M) and aerosol (β)) at a far-end reference height z_f. It is also assumed (3) that the aerosol optical and microphysical properties are constant from the ground up to the height z_o where the lidar system is estimated to achieve full overlap and (4) that the AOTs at the lidar wavelengths are retrieved from co-located in space and time AERONET measurements. Note that constrains (1)–(4) are common to LIRIC. In addition, LIRIC that is an algorithm for solving inverse problems, searches for particle lidar profiles that best match the AERONET-derived column volume concentrations, to retrieve the vertical profiles of fine $C_f(\lambda_i, z)$ and coarse $C_c(\lambda_i, z)$ particle volume concentrations.

Three case studies with different aerosol load scenarios have been analyzed to investigate the LIRIC retrieval ability. One case study deals with aerosol measurements affected by anthropogenic, biomass-burning, and soil particles. The second case study

AMTD
7, 8881–8926, 2014

deals with anthropogenic pollution likely affected by marine aerosol and the last one deals with aerosols significantly affected by Sahara dust. The comparison of the LIRIC extinction coefficient profiles with the corresponding profiles from the CII-procedure has revealed for all study cases, that the differences between $\alpha_L(\lambda_i, z)$ and $\alpha(\lambda_i, z)$ vary with altitude and wavelength and decrease with the increase of λ_i. The comparison of Ångstrom exponent profiles has revealed that the differences between $\mathring{A}_L(\lambda_1, \lambda_2, z)$ and $\mathring{A}(\lambda_1, \lambda_2, z)$ vary with z and the wavelength pair. Ångstrom exponents are good indicators of the dominant aerosol size; however, their sensitivity to the aerosol size varies with the wavelength pair. Hence, the Ångstrom exponent inter comparison has clearly indicated that the differences between $\mathring{A}_L(\lambda_1, \lambda_2, z)$ and $\mathring{A}(\lambda_1, \lambda_2, z)$ are mainly linked to the changes with z of the aerosol size distribution retrieved from LIRIC. The plot on the aerosol classification framework of the Ångstrom exponent spectral difference vs. the 355–1064 nm-Ångstrom exponent has revealed for all case studies that the data retrieved from LIRIC and the CII-procedure are on average on a framework area characterized by rather similar fine mode fraction values. However, LIRIC data are on average located on a curve with nearly constant fine modal radius while, the CII-procedure data points are spread on a framework region revealing that the fine modal radius is dependent on the altitude a.g.l. The results from the aerosol classification framework have also allowed inferring that the deviations between the LIRIC aerosol parameters and the corresponding CII-procedure aerosol parameters are mainly due to the fact that LIRIC does not allow to the modal radius of fine mode particles to vary with the altitude. In fact, the analysis of the three case studies has revealed that the differences between the aerosol products from LIRIC and the CII-procedure are quite large when aerosol from different sources and/or from different advection routes are located at the altitudes sounded by the lidar. To this end, it is worth noting that the analysis of the 12 September 2011 lidar measurements has revealed that the aerosol properties were weakly dependent on z within 1–3 km a.g.l., in accordance with the backtrajectory pathways. Then, we have found that the differences between the LIRIC aerosol products and the corresponding ones resulting from the CII-procedure were on average smaller

AMTD
7, 8881–8926, 2014

than the ones resulting from the other two study cases. However, one must be aware that several studies have revealed that aerosol from different sources and/or from different advection routes are commonly advected at different altitudes a.g.l. over the Central Mediterranea. So, the uncertainties of the LIRIC aerosol products may be large when the LIRIC method is applied to lidar measurements performed over the Mediterranean basin. In conclusion, the paper has contributed to the characterization of numerical procedures that allow determining the dependence on altitude of aerosol properties from multi wavelength elastic lidar signals. In particular, the paper has furthermore revealed the ability of the aerosol classification framework to estimate the dependence on altitude of the aerosol fine modal radius and of the fine mode fraction by the Ångstrom exponent spectral difference vs. the 355–1064 nm-Ångstrom exponent plot. We believe that the LIRIC retrieval ability could be improved by taking into account the results on the changes with z of the fine modal radius, resulting from the aerosol classification framework by using the Ångstrom exponent profiles retrieved from the CII-procedure. Work is on progress in this direction.

Acknowledgements. Work supported by the European Community through the ACTRIS Research Infrastructure Action under the 7th Framework Programme under ACTRIS Grant Agreement no 262254. The authors gratefully acknowledge G. P. Gobbi for providing the Å-ΔÅ aerosol classification frameworks. The authors would also like to acknowledge the NASA/Goddard Space Flight Center and the Barcelona Super-Computing Centre for their contribution with satellite images, and DREAM dust profiles, respectively. The authors gratefully acknowledge the NOAA Air Resources Laboratory (ARL) for the provision of the HYSPLIT backtrajectories used in this publication.

References

Ansmann, A., Seifert, P., Tesche, M., and Wandinger, U.: Profiling of fine and coarse particle mass: case studies of Saharan dust and Eyjafjallajökull/Grimsvötn volcanic plumes, Atmos. Chem. Phys., 12, 9399–9415, doi:10.5194/acp-12-9399-2012, 2012.

AMTD
7, 8881–8926, 2014

Barnaba, F., Tafuro, A. M., De Tomasi, F., and Perrone, M. R.: Observed and simulated vertically resolved optical properties of continental aerosols over southeastern Italy: a closure study, J. Geophys. Res., 112, D10203, doi:10.1029/2006JD007926, 2007.

Bergamo, A., Tafuro, A. M., Kinne, S., De Tomasi, F., and Perrone, M. R.: Monthly-averaged anthropogenic aerosol direct radiative forcing over the Mediterranean based on AERONET aerosol properties, Atmos. Chem. Phys., 8, 6995–7014, doi:10.5194/acp-8-6995-2008, 2008.

Chaikovsky, A., Dubovik, O., Goloub, P., Tanre, D., Pappalardo, G., Wandinger, U., Chaikovskaya, L., Denisov, S., Grudo, Y., Lopatsin, A., Karol, J., Lapyonok, T., Korol, M., Osipenko, F., Savitski, D., Slesar, A., Apituley, A., Alados Arboledas, L., Binietoglou, I., Kokkalis, P., Granados Munoz, M. J., Papayannis, A., Perrone, M. R., Pietruczuk, A., Pisani, G., Rocadenbosch, F., Sicard, M., De Tomasi, F., Wagner, J., Wang, X.: Algorithm and software for the retrieval of vertical aerosol properties using combined lidar/radiometer data: dissemination in EARLINET, Reviewed & Revised Papers of the 26th International Laser Radar Conference, 25–29 June, Porto Heli, Greece, Paper SO3-09, 2012.

De Tomasi, F. and Perrone, M. R.: Lidar measurements of tropospheric water vapor and aerosol profiles over southeastern Italy, J. Geophys. Res., 108, 4286–4297, 2003.

De Tomasi, F., Tafuro, A. M., and Perrone, M. R.: Height and seasonal dependence of aerosol optical properties over southeast Italy, J. Geophys. Res., 111, D10203, doi:10.1029/2005JD006779, 2006.

Draxler, R. R. and Rolph, G. D.: HYSPLIT (HYbrid Single-Particle Lagrangian Integrated Trajectory) model, available at: http://www.arl.noaa.gov/ready/hysplit4.html (last access: 20 May 2014), NOAA Air Resources Laboratory, Silver Spring, MD, 2003.

Dubovik, O.: Optimization of numerical inversion in photopolarimetric remote sensing, in: Photopolarimetry in Remote Sensing, edited by: Videen, G., Yatskiv, Y., and Mishchenko, M., Kluwer Academic Publishers, Dordrecht, the Netherlands, 65–106, 2004.

Dubovik, O. and King, M.: A flexible inversion algorithm for retrieval of aerosol optical properties from Sun and sky radiance measurements, J. Geophys. Res., 105, 20673–20696, doi:10.1029/2000JD900282, 2000.

Dubovik, O., Sinyuk, A., Lapyonok, T., Holben, B. N., Mishchenko, M., Yang, P., Eck, T. F., Volten, H., Munoz, O., Veihelmann, B., van der Zande, W. J., Leon, J.-F., Sorokin, M., and Slutsker, I.: Application of spheroid models to account for aerosol particle nonsphericity in

AMTD
7, 8881–8926, 2014

remote sensing of desert dust, J. Geophys. Res., 111, D11208, doi:10.1029/2005JD006619, 2006.
Gobbi, G. P., Kaufman, Y. J., Koren, I., and Eck, T. F.: Classification of aerosol properties derived from AERONET direct sun data, Atmos. Chem. Phys., 7, 453–458, doi:10.5194/acp-7-453-2007, 2007.
Holben, B.: AERONET – a federated instrument network and data archive for aerosol characterization, Remote Sens. Environ., 66, 1–16, 1998.
Kleidman, R. G., O'Neill, N.T, Remer, L. A., Kaufman, Y. J., Eck, T. F., Tanrè, D., Dubovik, O., Holben, B. N.: Comparison of Moderate Resolution Imaging Spectroradiometer (MODIS) and Aerosol Robotic Network (AERONET) remote-sensing retrievals of aerosol fine mode fraction over ocean, J. Geophys. Res., 110, D22205, doi:10.1029/2005JD005760, 2005.
Lopatin, A., Dubovik, O., Chaikovsky, A., Goloub, P., Lapyonok, T., Tanré, D., and Litvinov, P.: Enhancement of aerosol characterization using synergy of lidar and sun-photometer coincident observations: the GARRLiC algorithm, Atmos. Meas. Tech., 6, 2065–2088, doi:10.5194/amt-6-2065-2013, 2013.
Mamouri, R. E., Papayannis, A., Amiridis, V., Müller, D., Kokkalis, P., Rapsomanikis, S., Karageorgos, E. T., Tsaknakis, G., Nenes, A., Kazadzis, S., and Remoundaki, E.: Multi-wavelength Raman lidar, sun photometric and aircraft measurements in combination with inversion models for the estimation of the aerosol optical and physico-chemical properties over Athens, Greece, Atmos. Meas. Tech., 5, 1793–1808, doi:10.5194/amt-5-1793-2012, 2012.
Matthias, V., Balis, D., Bosenberg, J., Eixmann, R., Iarlori, M., Komguem, L., Mattis, I., Papayannis, A., Pappalardo, G., Perrone, M. R., and Wang, X.: Vertical aerosol distribution over Europe: statistical analysis of Raman lidar data from 10 European Aerosol Research Lidar Network (EARLINET) stations, J. Geophys. Res., 109, D18201, doi:10.1029/2004JD004638, 2004.
Müller, D., Veselovskii, I., Kolgotin, A, Tesche, M., Ansmann, A., and Dubovik, O.:Vertical profiles of pure dust and mixed smoke–dust plumes inferred from inversion of multiwavelength Raman/polarization lidar data and comparison to AERONET retrievals and in situ observations, Appl. Optics, 52, 3178–3202, 2013.
O'Neill, N. T., Eck, T. F., Smirnov, A., Holben, B. N., and Thulasiraman, S.: Spectral discrimination of coarse and fine mode optical depth, J. Geophys. Res., 108, 4559, doi:10.1029/2002JD002975, 2003.

AMTD
7, 8881–8926, 2014

Perrone, M. R., Tafuro, A. M., and Kinne, S.: Dust layer effects on the atmospheric radiative budget and heating rate profiles, Atmos. Environ., 59, 344–354, 2012.
Perrone, M. R., De Tomasi, F., and Gobbi, G. P.: Vertically resolved aerosol properties by multi-wavelength lidar measurements, Atmos. Chem. Phys., 14, 1185–1204, doi:10.5194/acp-14-1185-2014, 2014.
Seinfeld, J. H. and Pandis, S. N.: Atmospheric Chemistry and Physics: From Air Pollution to Climate Change, J. Wiley &Sons, INC, 1998.
Schuster, G. L., Dubovick, O., and Holben, B. N.: Angstrom exponent and bimodal aerosol size distributions, J. Geophys. Res., 111, D07207, doi:10.1029/2005JD006328, 2006.
Tafuro, A. M., Kinne, S., De Tomasi, F., and Perrone, M. R.: Annual cycle of aerosol direct radiative effect over southeast Italy and sensitivity studies, J. Geophys. Res., 112, D20202, doi:10.1029/2006JD008265, 2007.
Veselovskii, I., Dubovik, O., Kolgotin, A. Lapyonok, T., Di Girolamo, P., Summa, D., Whiteman, D. N., Mishchenko, M., and Tanre, D.: Application of randomly oriented spheroids for retrieval of dust particle parameters from multi-wavelength lidar measurements, J. Geophys. Res., 115, D21203, doi:10.1029/2010JD014139, 2010.
Veselovskii, I., Dubovik, O., Kolgotin, A., Korenskiy, M., Whiteman, D. N., Allakhverdiev, K., and Huseyinoglu, F.: Linear estimation of particle bulk parameters from multi-wavelength lidar measurements, Atmos. Meas. Tech., 5, 1135–1145, doi:10.5194/amt-5-1135-2012, 2012.
Wagner, R., Ajtai, T., Kandler, K., Lieke, K., Linke, C., Müller, T., Schnaiter, M., and Vragel, M.: Complex refractive indices of Saharan dust samples at visible and near UV wavelengths: a laboratory study, Atmos. Chem. Phys., 12, 2491–2512, doi:10.5194/acp-12-2491-2012, 2012.
Wagner, J., Ansmann, A., Wandinger, U., Seifert, P., Schwarz, A., Tesche, M., Chaikovsky, A., and Dubovik, O.: Evaluation of the Lidar/Radiometer Inversion Code (LIRIC) to determine microphysical properties of volcanic and desert dust, Atmos. Meas. Tech., 6, 1707–1724, doi:10.5194/amt-6-1707-2013, 2013.

AMTD
7, 8881–8926, 2014

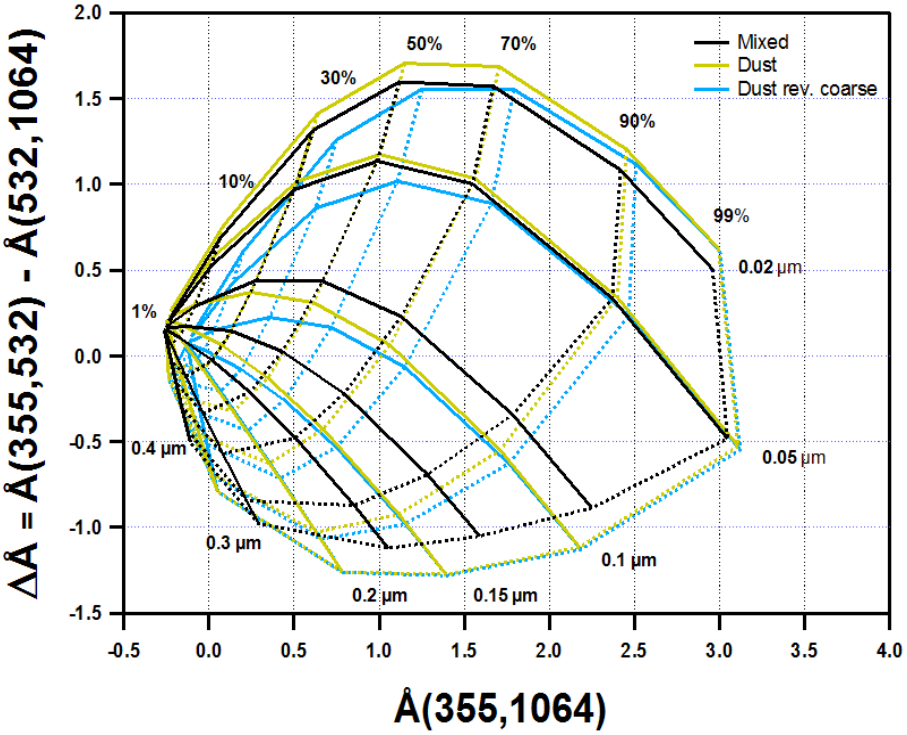

Figure 1. Aerosol classification framework calculated for mixed aerosol types (black lines) by setting $n = 1.455$ and $k = 0.0047$ at 532 nm, for desert dust particles (yellow lines) by setting $n = 1.55$ and $k = 0.008$ at 532 nm, and for large desert dust particles by setting the coarse modal radius equal to 0.75, 0.9, 0.105, and 0.12 µm (blue lines).

AMTD
7, 8881–8926, 2014

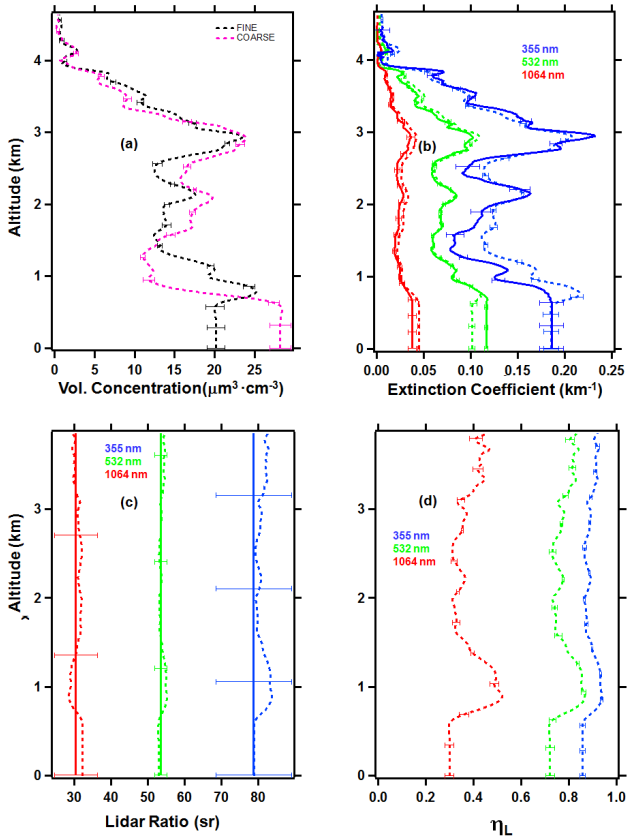

Figure 2. (a) Vertical profiles of the fine (black) and coarse (violet) particle volume concentrations with corresponding uncertainties retrieved from LIRIC by using lidar measurements performed on 29 August 2011 from 13:56 to 14:27 UTC. Vertical profiles of **(b)** extinction coefficients, **(c)** lidar ratios, and **(d)** fine mode fractions at 355 nm (blue), 532 nm (green), and 1064 nm (red) from LIRIC (dotted lines) and the constrained iterative procedure (solid lines) with corresponding uncertainties (error bars).

AMTD
7, 8881–8926, 2014

Profiling of fine- and coarse-mode particles with LIRIC (LIdar/Radiometer Inversion Code)

M. R. Perrone et al.

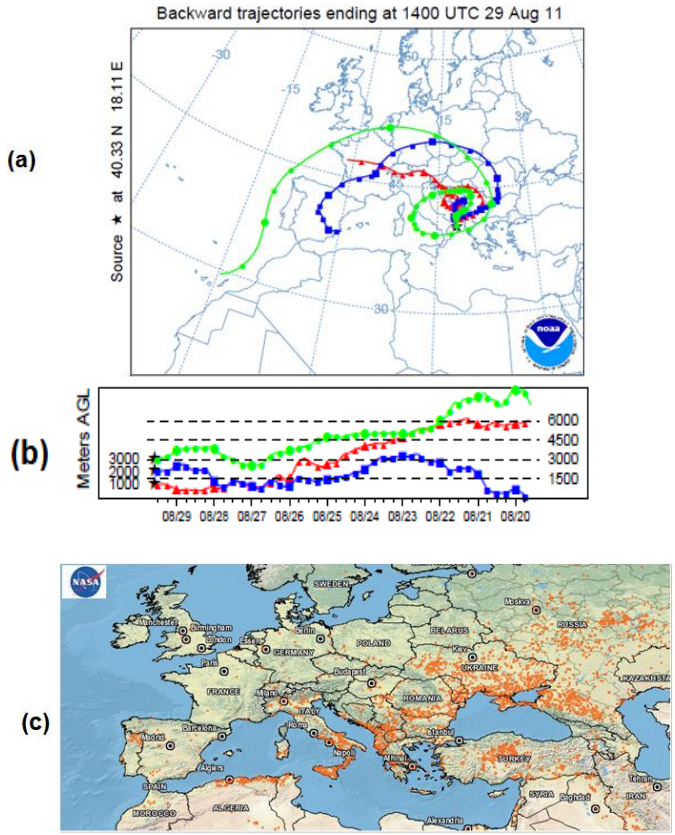

Figure 3. (a) Pathways estimated at 14:00 UTC of 29 August 2011, of the ten day HYSPLIT backtrajectories with arrival heights at 1, 2, and 3 km a.g.l. **(b)** Time evolution of the altitude of each backtrajectory. **(c)** 10 day fire map by MODIS from 20 to 29 August 2011 (http://rapidfire.sci.gsfc.nasa.gov/firemaps/).

AMTD
7, 8881–8926, 2014

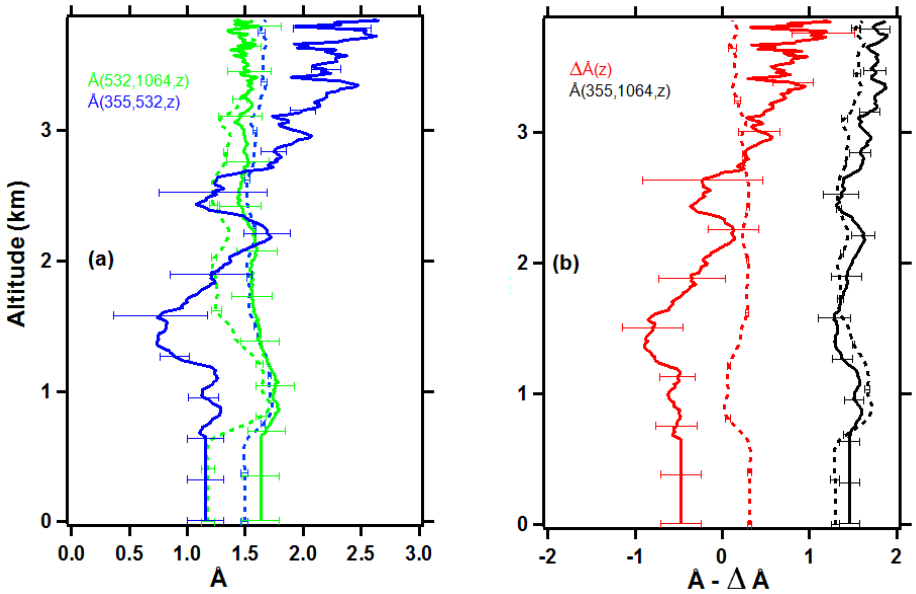

Figure 4. Vertical profiles of **(a)** Ångstrom exponents for different wavelength pairs and **(b)** of the 355–1064 nm Ångstrom exponent (black) and of the spectral difference (red) from LIRIC (dotted lines) and the constrained iterative inversion procedure (solid lines) with corresponding uncertainties (error bars).

AMTD
7, 8881–8926, 2014

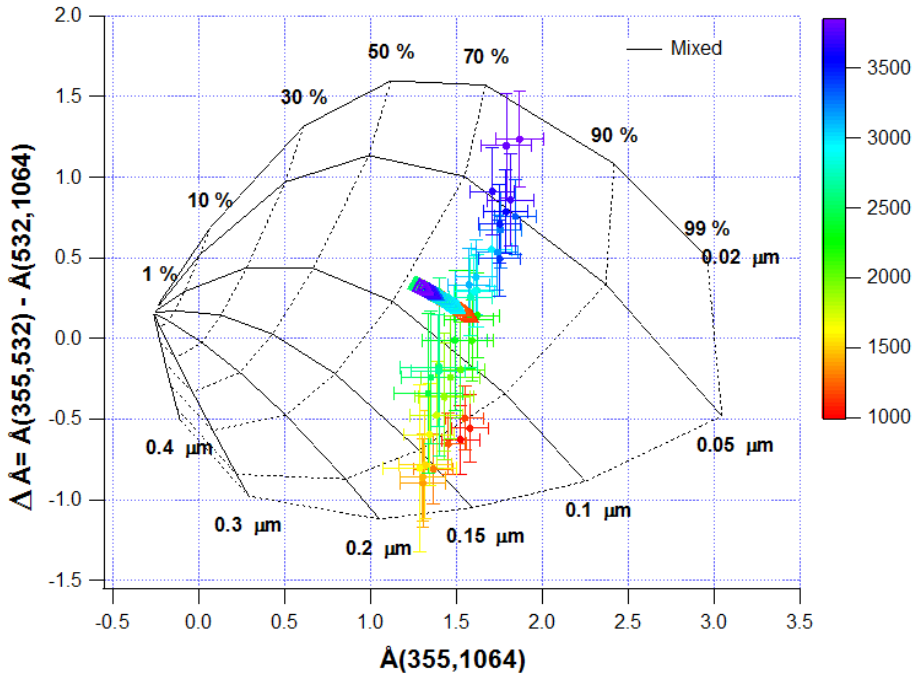

Figure 5. Solid and dashed black lines represent the graphical framework calculated for $n = 1.455$ and $k = 0.0047$ at 532 nm. Open triangles represent $\Delta\text{Å}_L(z)$ vs. $\text{Å}_L(355, 1064, z)$ mean values with corresponding uncertainties retrieved from LIRIC by using lidar measurements performed on 29 August 2011 from 13:56 to 14:27 UTC. Full dots represent $\Delta\text{Å}(z)$ vs. Å(355, 1064, z) mean values obtained from the CII-procedure. Error bars represent uncertainties. Different colors are used to represent values referring to different z, as indicated by the color bar on the right of the figure.

AMTD
7, 8881–8926, 2014

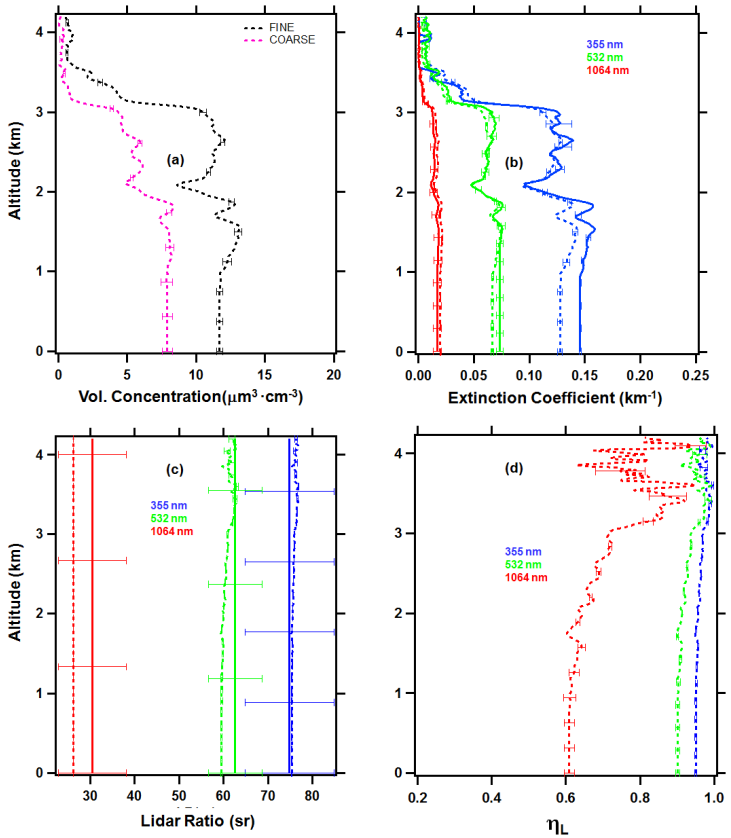

Figure 6. (a) Vertical profiles of the fine (black) and coarse (violet) particle volume concentrations with corresponding uncertainties retrieved from LIRIC by using lidar measurements performed on 12 September 2011 from 14:06 to 14:36 UTC. Vertical profiles of **(b)** extinction coefficients, **(c)** lidar ratios, and **(d)** fine mode fractions at 355 nm (blue), 532 nm (green), and 1064 nm (red) from LIRIC (dotted lines) and the constrained iterative procedure (solid lines) with corresponding uncertainties (error bars).

AMTD
7, 8881–8926, 2014

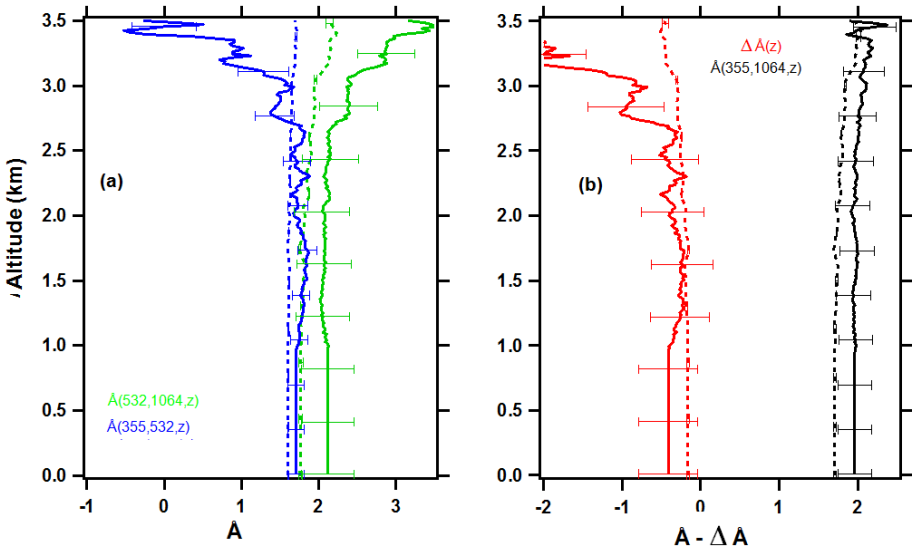

Figure 7. Vertical profiles of **(a)** Ångstrom exponents for different wavelength pairs and **(b)** of the 355–1064 nm Ångstrom exponent (black) and of the spectral difference (red) from LIRIC (dotted lines) and the constrained iterative inversion procedure (solid lines) with corresponding uncertainties (error bars).

AMTD
7, 8881–8926, 2014

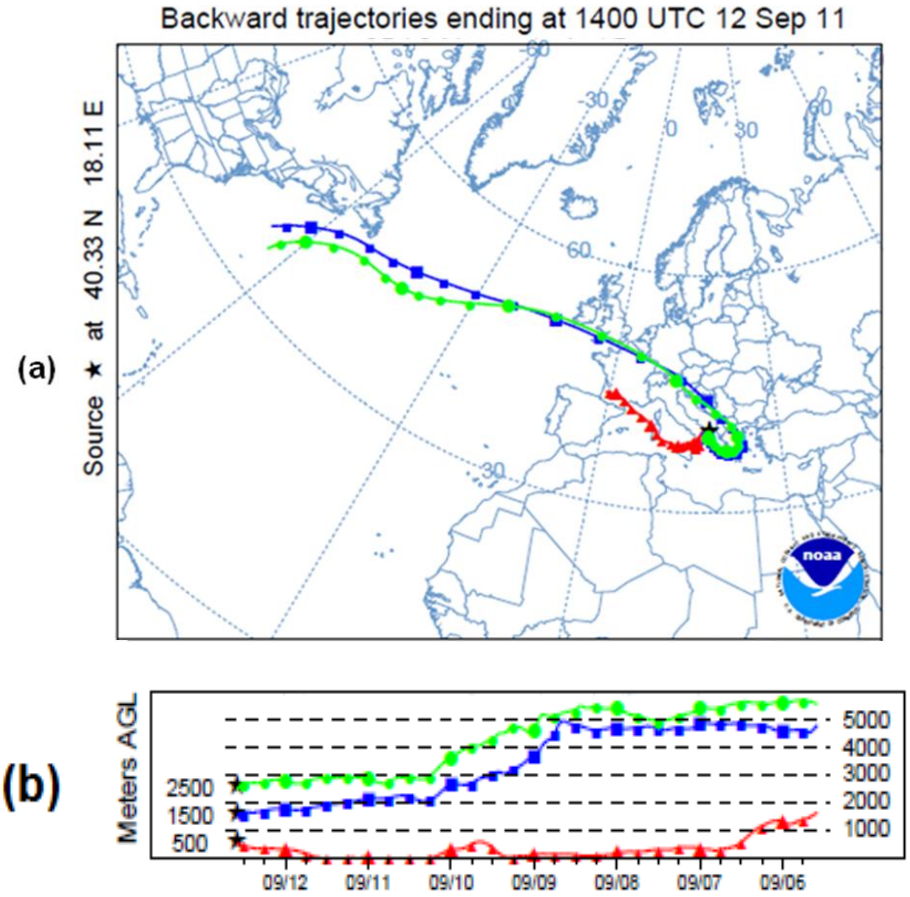

Figure 8. (a) Pathways estimated at 14:00 UTC of 12 September 2011, of the seven day HYSPLIT backtrajectories with arrival heights at 0.5, 1.5, and 2.5 km a.g.l. **(b)** Time evolution of the altitude of each backtrajectory.

AMTD
7, 8881–8926, 2014

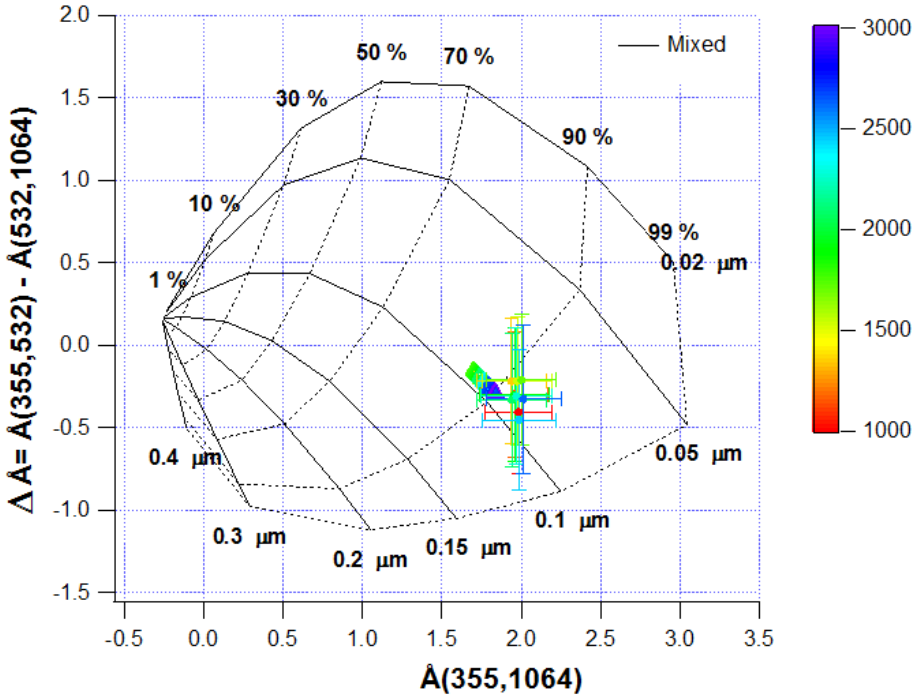

Figure 9. Solid and dashed black lines represent the graphical framework calculated for $n = 1.455$ and $k = 0.0047$ at 532 nm. Open triangles represent $\Delta\text{Å}_L(z)$ vs. $\text{Å}_L(355, 1064, z)$ values with corresponding uncertainties retrieved from LIRIC by using the lidar measurements performed on 12 September 2011 from 14:06 to 14:36 UTC. Full dots represent $\Delta\text{Å}(z)$ vs. Å(355, 1064, z) values from the CII-procedure. Error bars represent uncertainties. Different colors are used to represent values referring to different z, as indicated by the color bar on the right of the figure.

AMTD
7, 8881–8926, 2014

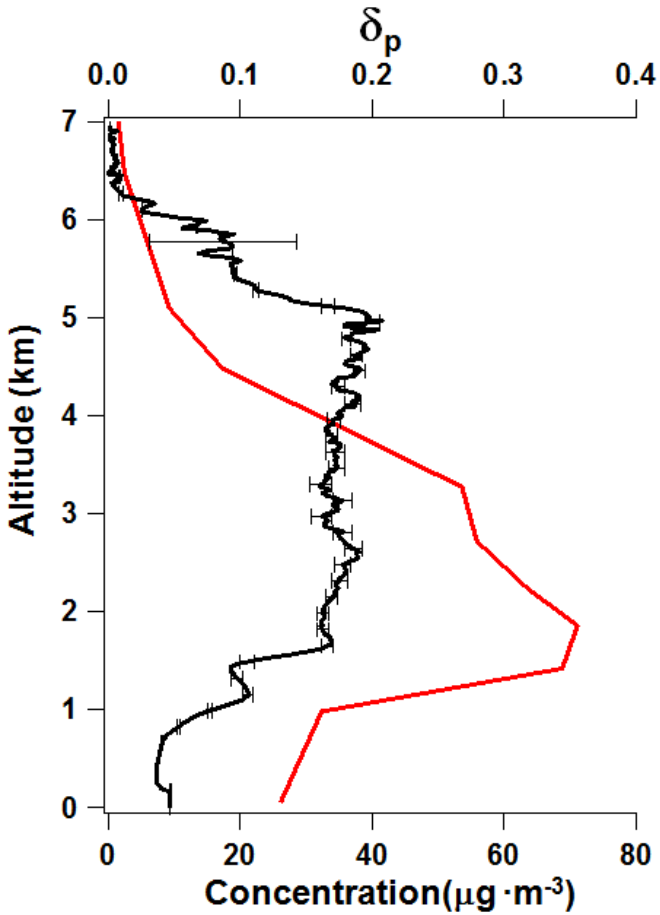

Figure 10. Vertical profile of the linear particle depolarization ratio (black line) and of the dust mass concentration simulated by the BSC-DREAM at 12:00 UTC of 6 August 2012.

AMTD
7, 8881–8926, 2014

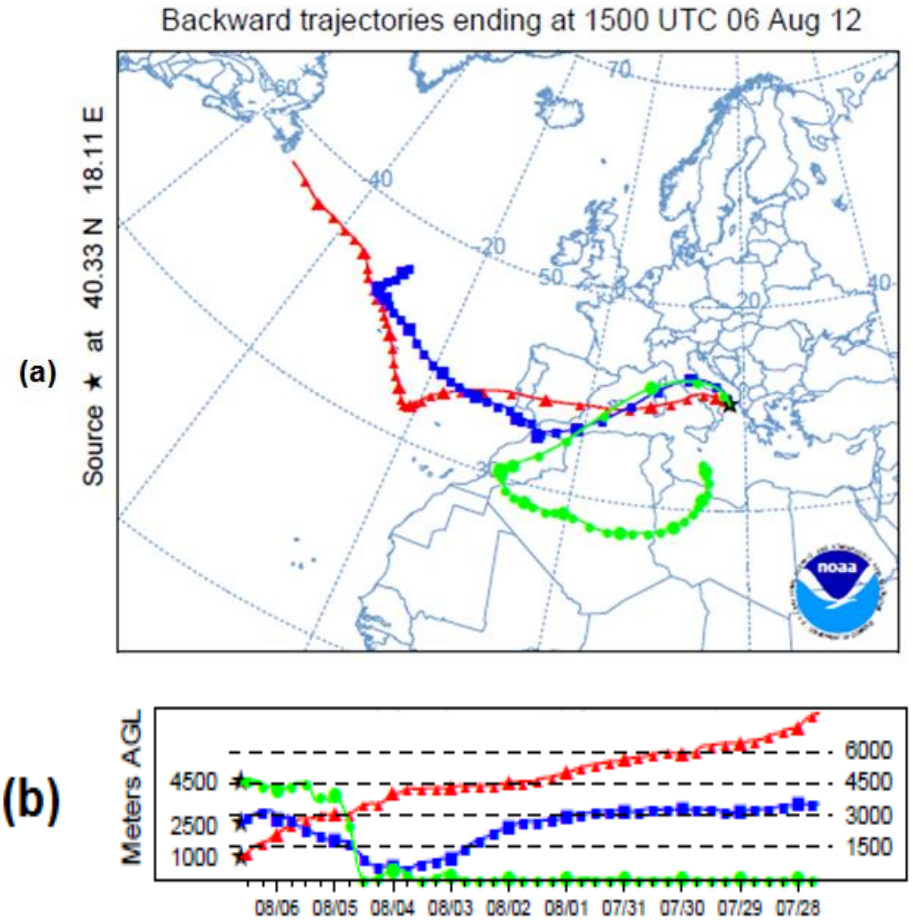

Figure 11. (a) Pathways estimated at 15:00 UTC of 6 August 2012, of the ten day HYSPLIT backtrajectories with arrival heights at 1, 2.5 and 4.5 km a.g.l. **(b)** Time evolution of the altitude of each backtrajectory.

AMTD
7, 8881–8926, 2014

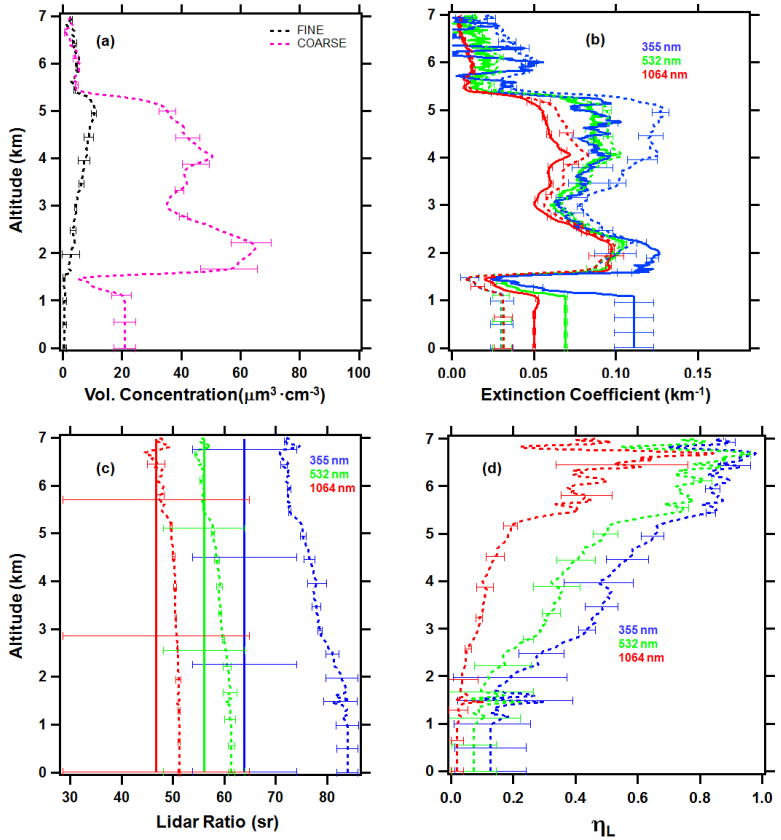

Figure 12. (a) Vertical profiles of the fine (black) and coarse (violet) particle volume concentrations with corresponding uncertainties retrieved from LIRIC by using lidar measurements performed on 6 August 2012 from 14:57 to 15:21 UTC. Vertical profiles of **(b)** extinction coefficients, **(c)** lidar ratios, and **(d)** fine mode fractions at 355 nm (blue), 532 nm (green), and 1064 nm (red) from LIRIC (dotted lines) and the constrained iterative procedure (solid lines) with corresponding uncertainties (error bars).

AMTD
7, 8881–8926, 2014

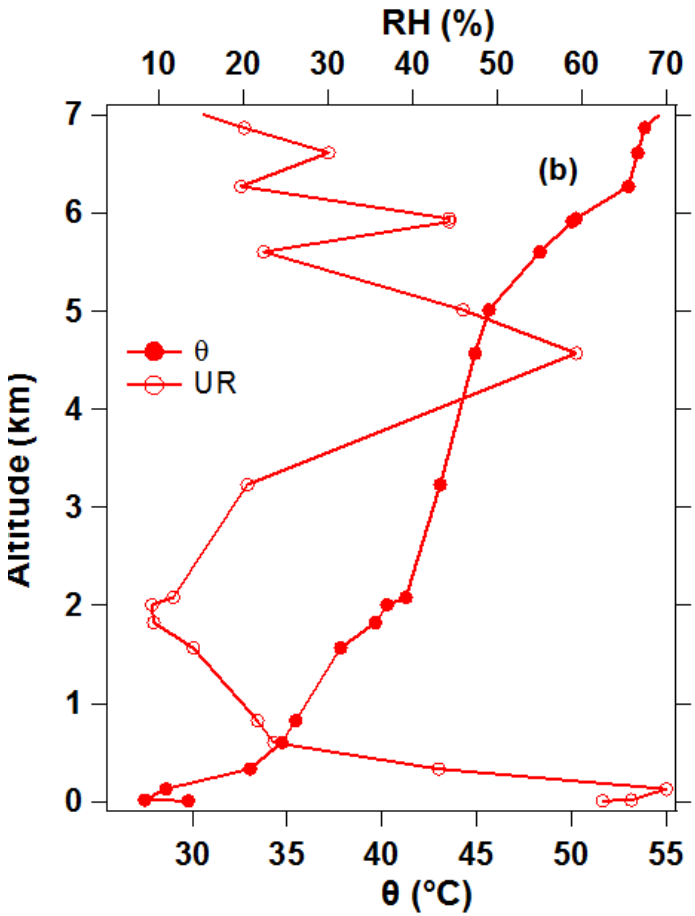

Figure 13. Vertical profiles of the potential temperature (θ) and relative humidity (RH) retrieved from radio sounding measurements performed on 6 August at 11:00 UTC.

AMTD
7, 8881–8926, 2014

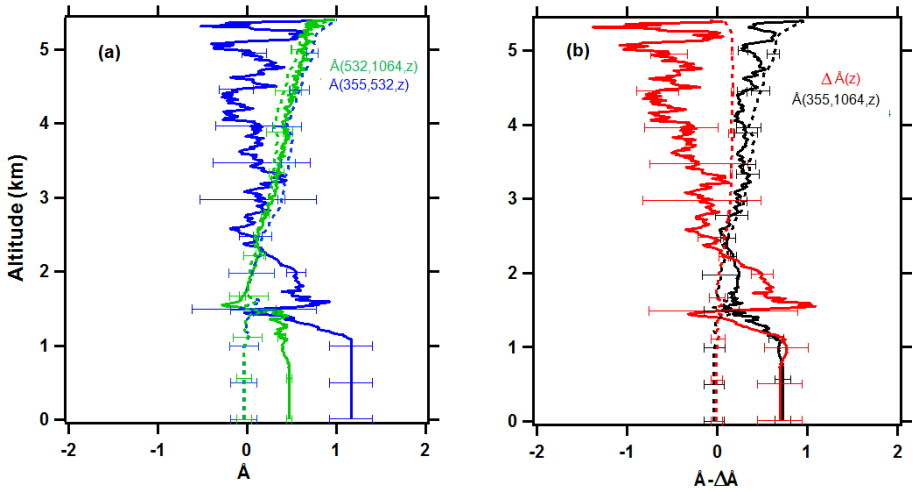

Figure 14. Vertical profiles of **(a)** Ångstrom exponents for different wavelength pairs and **(b)** of the 355–1064 nm Ångstrom exponent (black) and of the spectral difference (red) from LIRIC (dotted lines) and the constrained iterative inversion procedure (solid lines) with corresponding uncertainties (error bars).

AMTD
7, 8881–8926, 2014

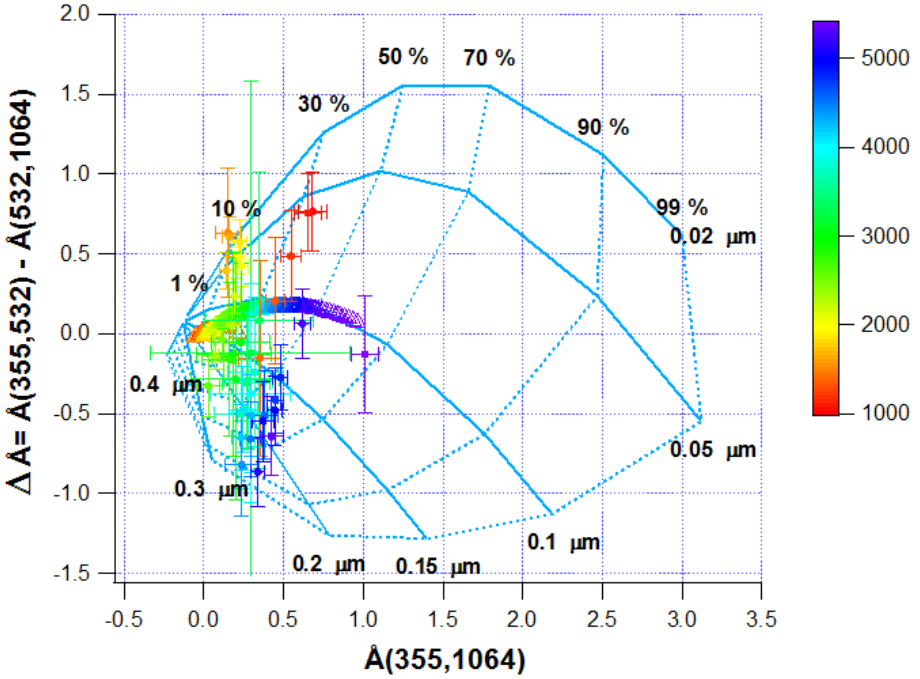

Figure 15. Solid and dashed black lines represent the graphical framework calculated for n = 1.55 and k = 0.008 at 532 nm and coarse mode radii $R_{c,GF}$ = 0.75, 0.9, 0.105, and 0.12 µm (Dust-rev framework). Open triangles represent $\Delta\text{Å}_L(z)$ vs. $\text{Å}_L(355, 1064, z)$ values with corresponding uncertainties from LIRIC by using the lidar measurements performed on 12 September 2011 from 14:06 to 14:36 UTC. Full dots represent $\Delta\text{Å}(z)$ vs. $\text{Å}(355, 1064, z)$ values. Error bars represent uncertainties. Different colors are used to represent values referring to different z, as indicated by the color bar on the rigth of the figure.

AMTD
7, 8881–8926, 2014